Electric Field Effect on Phospholipid Monolayers at an Aqueous–Organic Liquid–Liquid Interface

Hao Yu,[†] Irena Yzeiri,[‡] Binyang Hou,[†] Chiu-Hao Chen,[†] Wei Bu,[†] Petr Vanysek,[§] Yu-Sheng Chen,[∥] Binhua Lin,[∥] Petr Král,[†,‡] and Mark L. Schlossman*,[†]

[†]Department of Physics, University of Illinois at Chicago, Chicago, Illinois 60607, United States
[‡]Department of Chemistry, University of Illinois at Chicago, Chicago, Illinois 60607, United States
[§]Department of Chemistry & Biochemistry, Northern Illinois University, DeKalb, Illinois 60115, United States
[∥]The Center for Advanced Radiation Sources, University of Chicago, Chicago, Illinois 60637, United States

ABSTRACT: The electric potential difference across cell membranes, known as the membrane potential, plays an important role in the activation of many biological processes. To investigate the effect of the membrane potential on the molecular ordering of lipids within a biomimetic membrane, a self-assembled monolayer of 1-stearoyl-2-oleoyl-*sn*-glycero-3-phosphocholine (SOPC) lipids at an electrified 1,2-dichloroethane/water interface is studied with X-ray reflectivity and interfacial tension. Measurements over a range of electric potential differences, −150 to +130 mV, that encompass the range of typical biomembrane potentials demonstrate a nearly constant and stable structure whose lipid interfacial density is comparable to that found in other biomimetic membrane systems. Measurements at higher positive potentials, up to 330 mV, illustrate a monotonic decrease in the lipid interfacial density and accompanying variations in the interfacial configuration of the lipid. Molecular dynamics simulations, designed to mimic the experimental conditions, show that the measured changes in lipid configuration are due primarily to the variation in area per lipid with increasing applied electric field. Rotation of the SOPC dipole moment by the torque from the applied electric field appears to be negligible, except at the highest measured potentials. The simulations confirm in atomistic detail the measured potential-dependent characteristics of SOPC monolayers. Our hybrid study sheds light on phospholipid monolayer stability under different membrane potentials, which is important for understanding membrane processes. This study also illustrates the use of X-ray surface scattering to probe the ordering of surfactant monolayers at an electrified aqueous–organic liquid–liquid interface.
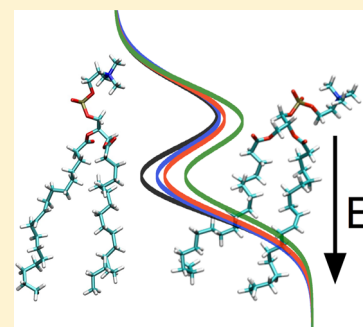
1. INTRODUCTION

It is well-known that the membrane potential influences the organization and functionality of cell membranes. For instance, membrane potentials on the order of 100 mV play a critical role in ATP synthesis.[1,2] Other examples include the opening and closing of A-type voltage-gated K$^+$ channels which occur at membrane potentials between −100 and +100 mV[3] and the destabilization of cholesterol–phospholipid complexes.[4] Direct effects on the integrity of the biomembrane, such as reversible permeabilization and electroporation, occur at higher membrane potentials.[5,6]

Lipid monolayers at the interface between immiscible aqueous and organic electrolyte solutions have been used as a model system for investigating electric field effects on membrane processes.[7−15] The lipids are dissolved in an organic electrolyte phase and self-assemble at the aqueous–organic liquid–liquid interface. The applied electric potential difference between aqueous and organic electrolyte solutions, $\Delta\phi^{w−o} = \phi^{water} − \phi^{organic}$, expresses the difference between the Galvani electric potentials far from the interface in the bulk aqueous phase, ϕ^{water}, and in the bulk organic phase, $\phi^{organic}$. Experiments on interfacial layers of phosphatidylcholine (PC) lipids have demonstrated low and nearly constant values of interfacial tension for a range of negative values of $\Delta\phi^{w−o}$, thus suggesting a nearly constant adsorption of lipids over this range of potentials.[8,13−16] Increasing $\Delta\phi^{w−o}$ to positive values led to an increase in interfacial tension. Several authors have suggested that interfacial PC lipids become positively charged by proton or cation binding at an appropriate positive value of $\Delta\phi^{w−o}$ and are subsequently desorbed from the interface into the bulk organic phase, thereby raising the interfacial tension.[13,14,16,17]

Complementary to these electrochemical studies of lipid monolayers at the aqueous–organic interface are electrochemical, fluorescence, and AFM force–distance studies of lipid monolayers at the mercury–aqueous liquid–liquid interface.[18−20] These studies have provided evidence for a series of conformational transitions of phospholipid layers that include pore formation and other structural transitions. At this interface, monolayers of dioleoylphosphatidylcholine (DOPC) are measured to be stable and unchanging over a range of potential differences that correspond to $\Delta\phi^{w−m} = \phi^{water} − \phi^{mercury}$ varying from −200 to +600 mV (note that the negative

of these potentials is usually quoted in the mercury–water literature).[20] Transitions occur at higher potential differences, starting at $\Delta\phi^{w-m} \approx 600$ mV, and are believed to be correlated with the penetration of ions from the aqueous phase through the lipid layer to rest against the mercury surface.[21] The range of $\Delta\phi^{w-m}$ for which unchanging, stable monolayers are observed at the mercury–aqueous interface spans the entire range of potential differences that are presented in this manuscript for which changes are observed at the aqueous–organic interface. The chemical environments for lipids at the two interfaces are quite different. The lipids are insoluble in mercury, and stable monolayers at the mercury–aqueous interface are believed to have the phospholipid tails adjacent to but not mixed with or penetrating into the mercury phase. In contrast, lipid monolayers at the aqueous–organic interface are Gibbs monolayers that self-assemble from lipids dissolved in the organic phase.

Molecular dynamics (MD) simulations have also been used to investigate the role of membrane potential on many essential biological processes. These include the study of the potential distribution throughout the membrane,[22] ion conduction and water transport through membranes,[23−26] ion channel gating,[27] conformational changes induced in membrane proteins,[28] and peptide insertion into membranes.[29,30] MD simulations of large membrane potentials of ~1−3 V reoriented the headgroup dipole moments in dioleoylphosphatidylcholine (DOPC) bilayers to induce electroporation.[31,32] Related simulations have shown that the effect of the transmembrane potential on the dipole moment of the PC headgroup contributes to reorientation of the entire dimyristoylphosphatidylcholine lipid during electroporation in lipid bilayers.[33]

These experimental and computational studies highlight two different aspects of phospholipid behavior at electrified interfaces that can alter phospholipid ordering at the interface: electric-potential-driven chemical binding or reactions and the torque imposed on the lipid dipole moment by the interfacial electric field. To further investigate these and other aspects of lipid ordering at an aqueous–organic electrified interface on the molecular length scale, we present a study that combines X-ray reflectivity measurements and molecular dynamics (MD) simulations of PC lipid layers at the electrified liquid–liquid interface. X-ray reflectivity probes the electron density profile perpendicular to the interface, which can be interpreted in terms of molecular ordering on the sub-nanometer length scale.[34] This technique has been used numerous times to investigate the ordering of lipid monolayers and lipid–protein interactions at the liquid–vapor interface, though not under conditions that allow for application of a controlled electric potential.[35−43] More recently, X-ray reflectivity has been applied to the study of surfactant and lipid ordering at oil–water interfaces, though the role of electrostatic interactions was not explored.[23,44−48] In these studies, X-ray reflectivity was used to characterize the thickness and electron density of the headgroup and tailgroup regions of the surfactant layers, which can be related to headgroup and tailgroup packing. This can lead to conclusions, for example, as to whether the tailgroups are all-trans and close-packed or disordered and loosely packed. Depending upon the system studied, conclusions can also be drawn about the penetration or adsorption of solvent molecules or electrolytes into the interfacial region occupied by the surfactant layer. X-ray reflectivity measurements are not likely to be sensitive to the orientation of a surfactant headgroup within a monolayer, because the orientation will not usually

have a significant effect on the electron density; nevertheless, X-ray reflectivity measurements of proteins bound to lipid monolayers have determined the extent of penetration of protein molecules into the lipid layer as well as the orientation of the protein.[38,39]

In the present work, X-ray reflectivity and electrochemistry studies of 1-stearoyl-2-oleoyl-*sn*-glycero-3-phosphocholine (SOPC) lipid monolayers are carried out on the liquid–liquid interface between aqueous (pH 7.2) and organic electrolyte solutions. Aqueous solutions of 100 mM NaCl in contact with PC lipid headgroups were used to model physiological conditions of the outer leaflet of the plasma membrane of eukaryotic cells.[49] Unsaturated lipids were chosen for study because of their prevalence in natural biomembranes[50] and their relevance for planned studies of electrostatic effects on lipid–protein interactions. In addition, it is known that these unsaturated lipids form homogeneous monolayers, in contrast to monolayers of saturated lipids that often exhibit domains.[38,51] The absence of domains simplifies the interpretation of X-ray reflectivity measurements which average over the in-plane footprint of the X-ray beam on the interface.[46]

The applied electric potential difference $\Delta\phi^{w-o}$ between the bulk electrolyte solutions was varied from −150 to 330 mV. Electrochemical cyclic voltammetry and interfacial tension measurements are consistent with results from prior studies on DPPC, L-R-lecithin, and egg-yolk phosphatidylcholine lipids.[8,13,14] X-ray reflectivity measurements probe the variation in lipid monolayer thickness and electron density profile with applied electric potential difference $\Delta\phi^{w-o}$. These measurements demonstrate that stable and reproducible SOPC monolayers are formed with interfacial densities that can be varied from the high densities typical of unsaturated lipids in biomembranes[52] (~70 Å² per lipid molecule) to densities lower by about a factor of 2. Importantly, stable high density monolayers are observed with essentially unchanged structure over the range from −150 to +130 mV that is often relevant to physiological conditions. These data do not confirm a recent report of a 2 Å thinning of a tethered bilayer of POPC lipids studied by neutron reflectivity when the transbilayer voltage was varied between 0 and 100 mV.[53]

MD simulations were performed for controlled variations of lipid interfacial density and electric field amplitude. Variations in monolayer thickness and electron density of the headgroup and tailgroup agree with the results of X-ray reflectivity. MD simulations also reveal that variations in the lipid configuration, such as the angular orientation of the lipid, are determined primarily by the lipid interfacial density and not by the electric field torque on the lipid dipole moment. The results of our X-ray reflectivity measurements and MD simulations, which characterize the ordering on the molecular length scale of a PC lipid layer subject to an electric field, are qualitatively consistent with the previously reported chemical-reaction-driven adsorption/desorption process of interfacial lipid molecules.[13,14,17]
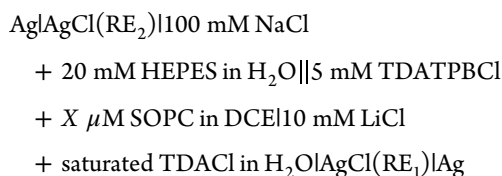
2. MATERIALS AND METHODS

2.1. Materials. The unsaturated phospholipid 1-stearoyl-2-oleoyl-*sn*-glycero-3-phosphocholine (SOPC, $C_{44}H_{86}NO_8P$, CAS# 56421-10-4) was used as received from Avanti Lipids. The aqueous electrolytes, NaCl (Alfa Aesar Puratronic, 99.999%, metals basis) and LiCl (certified ACS, crystal from Fisher Scientific Company), were roasted at 450 °C for 45 min to remove organic contaminants and water. Water from a Nanopure UV Barnstead system was used to prepare aqueous

alkali chloride solutions. HEPES buffer solution (1 M) was purchased from Fisher Scientific. 1,2-Dichloroethane (DCE, CHROMASOLV, for HPLC, 99.8%) was purchased from Sigma-Aldrich and purified by passing it six times through a column of activated basic alumina. DCE was further filtered through a 0.2 μm Millipore filter (OMNIPORE membrane filter, PTFE) using a stainless steel pressure filter holder (Sartorius-Stedim Biotech 16249), to remove residual alumina. The organic electrolytes tetradodecylammonium tetrakis(4-chlorophenyl)borate (TDATPBCl) and tetradodecylammonium chloride (TDACl, >97%) were used as received from Aldrich. 1-Hexadecanethiol (99%) was purchased from Sigma-Aldrich and used as received.

A concentrated SOPC stock solution was prepared by dissolving about 25 mg of SOPC into 250 mL of DCE. It was stored in a refrigerator prior to further use within 1 month. A concentrated TDATPBCl stock solution was prepared from DCE and then saturated with water by placing it in contact with a few mL of pure water and rocking the solution for about 12 h.[54] This solution was then filtered through a 0.2 μm Millipore filter, as described above. Organic solutions used in the experiments were prepared by diluting the concentrated TDATPBCl and SOPC stock solutions with pure DCE. The saturated TDACl solution placed in contact with one of the reference electrodes is prepared by soaking 100 mg of TDACl in a gently shaken flask containing 100 mL of 10 mM LiCl aqueous solution. Sodium chloride was dissolved in water and mixed with 1 M HEPES aqueous buffer solution to produce a pH 7.2 aqueous solution with 100 mM NaCl and 20 mM HEPES. This solution was saturated with DCE by placing it in contact with a few mL of purified DCE, rocking the solution for about 12 h,[54] and then filtering it through a Millipore filter, as described above.

2.2. Liquid−Liquid Electrochemical Sample Cell. Figure 1 is a schematic of the four-electrode electrochemical cell used for all reported measurements. The electric current and potential difference across the electrochemical cell can be measured and precisely controlled, and the interfacial tension measured concurrently with X-ray reflectivity measurements.

The galvanic cell is represented by the following scheme:

Ag|AgCl(RE$_2$)|100 mM NaCl

     + 20 mM HEPES in H$_2$O‖5 mM TDATPBCl

     + X μM SOPC in DCE|10 mM LiCl

     + saturated TDACl in H$_2$O|AgCl(RE$_1$)|Ag

where ‖ represents the interface of interest and X is varied from 0 to 12.5. The aqueous and organic electrolyte solutions are electrically conductive; therefore, the external potential across the interface can be controlled electrochemically to investigate the lipid monolayer response to electric potential differences between the adjacent bulk solutions. Two platinum meshes (platinum gauze, 52 mesh woven from 0.1 mm diameter wire, 99.9% metals basis, purchased from Alfa Aesar) are used as counter electrodes. The meshes are large, ∼25 cm^2, to ensure that the electric field is uniform across the plane of the interface. The mesh in the top aqueous phase is positioned ∼1 cm from the interface; the mesh in the bottom organic phase is ∼1.5 cm from the interface. Ag|AgCl reference electrodes placed in Luggin capillaries located within a few mm of the interface are used to monitor the electric potential difference across the interface. The reference electrode in the Luggin
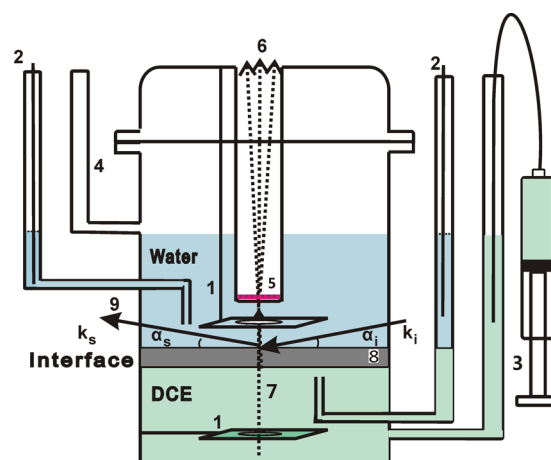
Figure 1. Illustration of the glass sample cell and X-ray kinematics. The flat circular DCE−water interface has an area of about 38.5 cm^2 (7 cm inner diameter of the glass cell). The lower part of the sample is made from a glass cylinder with a 1 mm thick wall. (1) Counter electrodes consist of platinum wires attached to square platinum mesh (CE$_{1,2}$). (2) Reference electrodes (RE$_{1,2}$) are AgCl coated Ag wires placed in Luggin capillaries that extend to ∼3 mm of the liquid−liquid interface. Adjusting the volume of the lower DCE phase with a syringe (3) flattens the interface. (4) Pressure release to maintain atmospheric pressure within the cell. (5) Optical grating for quasi-elastic light scattering (QELS) measurements of interfacial tension. (6) Dashed lines indicate the diffracted laser beam used to measure interfacial tension with QELS. (7) Laser beam for QELS measurements of interfacial tension (enters from the bottom of the cell). The liquid−liquid interface is pinned by the top edge of a strip of Mylar (8), coated as described in the text, which is pressed against the inside of the lower cylindrical part of the glass cell with a strip of stainless spring steel. (9) X-rays pass though the side walls of the cell and traverse the upper aqueous solution to reflect off the liquid−liquid interface.

capillary connected to the DCE phase is immersed in a 10 mM LiCl and saturated TDACl conductive aqueous solution. The applied electric potential difference is controlled and recorded by a Solartron 1287 (Solartron Instruments, England). The electric potential difference across the galvanic cell, as measured by the Solartron 1287, is denoted $\Delta\phi_{cell}^{w-o}$. We adopt the rational potential scale[55,56] that approximates the electric potential difference $\Delta\phi^{w-o} = \phi^{water} - \phi^{oil}$ between the aqueous and organic bulk phases (far from interfaces and electrodes) as $\Delta\phi^{w-o} = \Delta\phi_{cell}^{w-o} - \Delta\phi_{pzc}^{w-o}$, where the potential of zero charge, $\Delta\phi_{pzc}^{w-o} = 0.167$ V, is determined from the apex of the electrocapillary curve measured for a sample without SOPC lipids.

A glass tube sealed with a float glass bottom extends downward from the cap and is immersed in the water phase to provide a path for the laser beam used for quasi-elastic light scattering (QELS) measurements of interfacial tension. A 1 cm diameter hole in the middle of each Pt mesh allows for passage of this laser beam. Comparative X-ray reflectivity measurements with and without this hole were similar, indicating that the presence of the hole had a negligible effect on the interfacial structure. Similarly, tension measurements from sample cells with Pt meshes that had smaller holes (∼3 mm in diameter) were identical.

X-ray reflectivity measurements require a very flat interface. Pinning the interface to the cell wall and adjusting the volume of the lower DCE phase accomplishes this. The interface can be pinned by the top edge of a hydrophobic strip when the cell

glass is hydrophilic. The cell was soaked in concentrated (98%) sulfuric acid solution of ammonium persulfate (18 g/L of H_2SO_4) for 5 h to render it hydrophilic. In previous experiments that studied the interfacial distribution of just the supporting electrolytes, a Teflon strip was used to pin the interface.[57−59] In the presence of interfacial SOPC lipids, the Teflon strip proved inadequate to pin the interface. Instead, the interface was pinned to the top edge of a hydrophobic gold-coated strip of Mylar prepared as follows. After evaporation of a 100 nm thick gold layer onto a 1.5 cm wide by 20 cm long strip of 0.18 mm thick Mylar (purchased from ePLASTICS), a 1-hexadecanethiol layer was self-assembled on the gold by immersing the Mylar strip in 4 mM 1-hexadecanethiol for 2 days under an argon or nitrogen atmosphere. The Mylar strip was pressed against the inside of the glass cell with a thin strip of stainless steel (Figure 1) and its upper edge positioned vertically midway between the ends of the Luggin capillaries. Once the interface is pinned by the top edge of the Mylar strip, adjusting the volume of the bottom phase with a syringe (Figure 1) and leveling the cell along axes parallel and perpendicular to the incident X-ray beam with a tilt stage produces a flat interface.

2.3. Interfacial Tension Measurements. Quasi-elastic light scattering (QELS) has been used to examine the dispersion relation between the frequency and surface wave-number of capillary waves and to measure the surface and interfacial tension γ of liquids.[60−63] This technique can measure the interfacial tension concurrently with X-ray reflectivity because it does not disturb the flatness of the interface. A home-built quasi-elastic light scattering (QELS) apparatus, sketched in Figure 2,[63] was used to measure the interfacial tension γ.
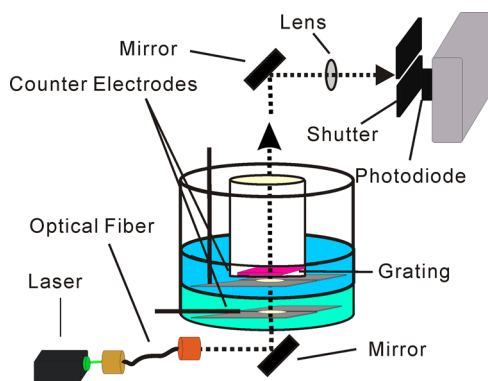
Figure 2. Illustration of the quasi-elastic light scattering (QELS) apparatus. A green Nd:YAG laser (wavelength 532 nm, 25 mW, Crystal Laser Corp.) is transmitted through the liquid−liquid interface and then scattered from a grating. The optical heterodyne signal incident on a photodiode was fed into a wide-band amplifier and then Fourier transformed.

The combination of laser light scattered from the interface and from a diffraction grating produced an optical heterodyne signal that was measured by a photodiode (S1133 Hamamatsu). Amplification of the photodiode signal by a wide-band amplifier (13AMP005 Melles Griot) and electronic fast Fourier transforming by an FFT analyzer (SRS760 Stanford Research) yielded a QELS spectrum containing a peak whose frequency depended on the selected order of the diffracted light. The grating was fabricated in the Nano Core Facility of the University of Illinois at Chicago by evaporating chromium onto

float glass to produce stripes 20 μm wide separated by 230 μm to yield a grating constant of $d = 250$ μm. Interfacial tension is determined by the peak frequency, according to[63−65]

$$f_p \approx f_c - \frac{f_c^{1/2} k[(\rho_w \eta_w)^{1/2} + (\rho_o \eta_o)^{1/2}]}{4\sqrt{\pi}(\rho_w + \rho_o)} \tag{1}$$

where $f_c^2 = \gamma k^3/[(2\pi)^2(\rho_o + \rho_w)]$, $\rho_w = 0.997 \times 10^3$ kg m^{-3} is the mass density of water, $\rho_o = 1.246 \times 10^3$ kg m^{-3} is the mass density of DCE, $\eta_w = 0.89 \times 10^{-3}$ kg m^{-1} s^{-1} is the viscosity of water, $\eta_o = 0.78 \times 10^{-3}$ kg m^{-1} s^{-1} is the viscosity of DCE, and the wavenumber $k = 2\pi n/d$ is calculated from the experimentally selected diffraction order n and the grating constant d. QELS spectra are fit to a Lorentzian function, $g(f) = 2\Gamma/[4\pi(f - f_p)^2 + \pi\Gamma^2]$, to determine the peak frequency f_p.

2.4. X-ray Reflectivity Measurements. X-ray reflectivity data were measured at the ChemMatCARS beamline 15-ID at the Advanced Photon Source (Argonne National Laboratory, USA) with a liquid surface reflectometer and measurement techniques described in detail elsewhere.[34,44,54] The reflectivity data were measured as a function of wave vector transfer perpendicular to the interface, $Q_z = (4\pi/\lambda) \sin \alpha_i$, where $\lambda = 0.4133 \pm 0.00005$ Å is the X-ray wavelength of ∼30 keV X-rays and α_i is the angle of incidence that is equal to the angle of reflection α_S (Figure 1). The in-plane components of the wave vector for specular reflection are given by $Q_x = Q_y = 0$. The size of the beam (∼0.018 × 3 mm^2, height by width) incident on the sample was set by a rectangular aperture (0.015 × 3 mm^2, height by width) positioned 68 cm before the sample. Reflected X-rays were recorded by a CCD detector (Bruker APEXII) placed 3.19 m from the sample center. Two slits were positioned between the sample and CCD. A slit with a 5 mm vertical gap was positioned 0.5 m in front of the CCD to reduce excess intensity on the CCD and block the beam transmitted through the interface. Its vertical position tracked the reflected X-ray beam. A second slit of dimensions 1 × 4 mm^2 was positioned 685.8 mm downstream of the sample center to reduce background scattering. The specularly reflected beam intensity is measured by summing over a region of 30 × 60 (height × width) virtual pixels (1.8 × 3.6 mm^2), whose center is determined by a two-dimensional Gaussian function fit to the signal. Background is measured as the average integrated intensity over two similar regions displaced 0.1° horizontally from the specular reflection. The reflectivity is calculated by subtracting the measured background intensity from the specular beam intensity, and then normalizing to the incident beam intensity measured by a detector placed before the sample.

2.5. Molecular Dynamics Simulations. *2.5.1. Methodology.* Atomistic molecular dynamics (MD) simulations were performed with NAMD, the TIP3P model for water, the CHARMM36 force field for lipids, and the CHARMM27 force field for everything else.[66−69] Nonbonding van der Waals (vdW) coupling between the ith and jth atoms is described by Lennard-Jones potentials. The short-range cutoffs for Coulombic and vdW interactions are, respectively, 10 and 12 Å. The time step is 1 fs. Langevin dynamics with a damping coefficient of 0.01 ps^{-1} sped up the simulations.[70,71] The particle mesh Ewald summation method (PME) was used for electrostatic interactions.[72] Simulations were run for 200−250 ns to reach a steady state interfacial structure. The NAP_zT ($P = 1$ atm, $T = 300$ K) ensemble was used with constant area in the $x-y$ plane and periodic boundary conditions in z. Under constant area

simulations, the $x-y$ simulation cell parameters and thus the lipid density are kept constant at values that match experimental values. Fluctuations of the simulation box size occur only in the z direction and the total height Z of the box was determined at the end of the simulation. A uniform electric field was applied in the z-direction to every charge in the simulation cell.[73]

2.5.2. Systems. Simulated systems consist of 50 NaCl, 50 BTPPATPBCl, 200 SOPC, 20496 water, and 8588 DCE molecules arranged within five layers in the following order: (1) aqueous solution (200 mM NaCl), (2) SOPC monolayer (100 SOPC lipids), (3) DCE solution (200 mM BTPPA$^+$/TPBCl$^-$ (bis-triphenylphosphoranylidene/tetrakis(4-chlorophenyl)-borate)), (4) SOPC monolayer (100 SOPC lipids), (5) aqueous solution (200 mM NaCl). We present results for only the top SOPC monolayer; the bottom monolayer prevents mixing of the solvents and improves system stability. In the absence of an applied electric field, the bottom half of the unit cell is practically a mirror image of the top. This is no longer true when an electric field is applied in the direction perpendicular to the lipid monolayer. In addition, significant monolayer curvature out of the $x-y$ plane is inhibited by the application of a small force (0.2 kcal/mol/Å) on the C2 carbon of each lipid (as shown later in Figure 9).

The choice of systems with different areas per lipid and applied electric fields (see Table 1) was guided by experimental

Table 1. Simulation Systems[a]

area per lipid (Å^2)	unit cell ($X \times Y \times Z$) (Å^3)	electric field (kcal mol^{-1} Å^{-1} e^{-1})	electric potential difference (V)
72.25	($85 \times 85 \times 288$)	−0.01839	−0.12
72.25	($85 \times 85 \times 288$)	0.00000	0.00
81.00	($90 \times 90 \times 260$)	0.03095	0.23
90.25	($95 \times 95 \times 233$)	0.03947	0.28
121.00	($110 \times 110 \times 175$)	0.07200	0.33

[a]The simulation electric field has units of 1 kcal mol^{-1} Å^{-1} e^{-1} ≈ 4.2 × 10^8 V m^{-1}. Determination of the electric potential difference will be discussed in section 3.5.

conditions. The organic cation BTPPA$^+$ was used in place of the experimental cation TDA$^+$ to reduce simulation time. Under conditions of positive electric potential difference, $\Delta\phi^{w-o} > 0$, organic cations are depleted from the region adjacent to the lipid monolayer. Therefore, organic cations only influence the potential drop in the DCE phase and use of a slightly different cation in the organic solvent should not significantly affect our results.

3. RESULTS AND ANALYSIS

3.1. Cyclic Voltammetry.
Figure 3 shows the cyclic voltammograms for liquid−liquid interfaces between DCE and aqueous electrolyte solutions with and without SOPC lipids dissolved in the DCE phase. The high current at the positive and negative edges of the potential windows is due to transport of supporting electrolytes across the aqueous−organic interface. Excess current is observed for $\Delta\phi^{w-o} > 0.1$ V when SOPC is in the DCE phase. Similar observations of excess current using other PC lipids have been attributed to lipids leaving the interface and redissolving in the bulk DCE phase.[15] Currents are much lower during X-ray reflectivity and interfacial tension measurements because the voltage ramping rate is lower, 1 mV s^{-1}, and the measurements take place after a
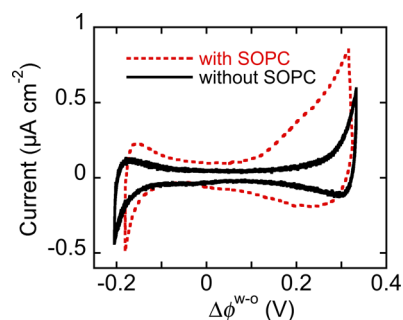
Figure 3. Cyclic voltammograms measured at a scan rate of 5 mV s^{-1} for interfaces between an aqueous solution of 100 mM NaCl + 20 mM HEPES (pH 7.2) and a DCE solution of 5 mM TDATPBCl in the absence (black solid line, 3 cycles) and presence (red dashed line, 1 cycle) of 3 μM SOPC in the DCE phase. The electric potential difference $\Delta\phi^{w-o} = \Delta\phi^{w-o}_{cell} - \Delta\phi^{w-o}_{pzc}$ is the difference between the potential difference applied across the galvanic cell $\Delta\phi^{w-o}_{cell}$ and the potential of zero charge $\Delta\phi^{w-o}_{pzc} = 0.167$ V.

period of relaxation to a steady state. The maximum electric potential differences for X-ray reflectivity measurements were chosen to limit the maximum currents to 0.13 μA cm^{-2} to reduce the effect of ion transport on these measurements. Typical values of relaxed currents in the central part of the potential window were 0.026 μA cm^{-2}.

3.2. Interfacial Tension Measurements.
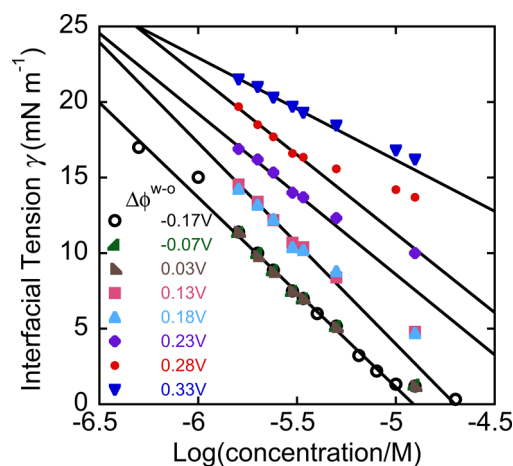Figure 4 shows the interfacial tension γ as a function of electric potential
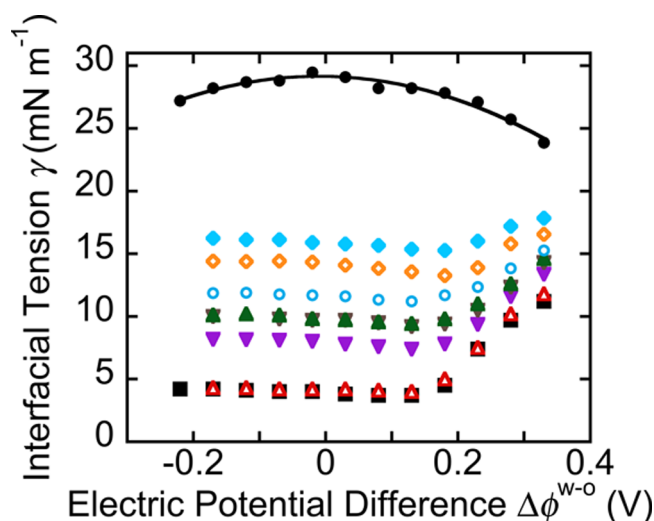
Figure 4. Electrocapillary curves (interfacial tension γ as a function of electric potential difference $\Delta\phi^{w-o}$) measured at $T \approx 23$ °C for interfaces between a DCE solution of X μM SOPC and 5 mM TDATPBCl and an aqueous solution of 0.1 M NaCl and 20 mM HEPES, with SOPC concentrations (in μM, top to bottom) of $X = 0$ (●, black), 1.6 (◆, blue), 2 (◇, orange), 2.4 (○, blue), 3 (▲, green), 3.4 (▽, black), 5 (▼, purple), 10 (△, red), 12.5 (■, black).

difference $\Delta\phi^{w-o} = \Delta\phi^{w-o}_{cell} - \Delta\phi^{w-o}_{pzc}$, i.e., the electrocapillary curve, for samples with different concentrations of SOPC in the DCE phase. The upper curve, measured in the absence of SOPC from a sample containing only the supporting electrolytes, is analyzed by Lippmann's equation to determine the potential of zero charge, $\Delta\phi^{w-o}_{pzc} = 0.167 \pm 0.008$ V. According to Lippmann's equation,[74] the excess charge per unit area of the interface $Q_{tot}(\Delta\phi^{w-o})$ is expressed as $Q_{tot}(\Delta\phi^{w-o}) =$

$-(\partial y/\partial \Delta\phi^{w-o})_{T,p,\mu_i}$, where T is the thermodynamic temperature, p is the external pressure, and μ_i is the chemical potential of species i. As described previously, a hyperbolic cosine describes the data well enough to determine the potential of zero charge, $\Delta\phi^{w-o}_{pzc}$, for which $Q_{tot}(\Delta\phi^{w-o}) = 0$.[59]

The other curves in Figure 4 show that the interfacial tension γ for a fixed concentration of SOPC is nearly constant below ~0.15 V but increases above 0.15 V. This variation in γ is reversible. Other authors have reported qualitatively similar variations in interfacial tension for other lipids at the electrified liquid–liquid interface.[13,15,16,75,76] These authors have suggested that the region of nearly constant interfacial tension corresponds to a stable monolayer of PC lipids in their zwitterionic form, and the region of increasing tension represents cationic PC lipids whose phosphate group has been neutralized by either protons or other aqueous cations. It has been further suggested that the cationic form of PC lipids can transfer protons or other cations from the aqueous phase into the organic phase, thereby reducing the interfacial concentration of lipids and raising the interfacial tension.[76,77]

The surface excess or adsorption of SOPC at the interface can be calculated from the variation of γ with sample concentration, according to $(\partial\gamma/\partial \ln c)_{\Delta\phi^{w-o},\mu_i,T,p} = -RT\Gamma$, where Γ is the Gibbs surface excess of SOPC, c is the mole fraction of SOPC, R is the gas constant, and the concentrations of all other components are held constant.[76] In spite of the presence of multiple components in our system, a full thermodynamic analysis shows that the variation of tension with lipid concentration leads to the standard Gibbs equation for lipid surface excess.[14] The linear relation between γ and $\log(C/M)$, where C is the molar concentration shown in Figure 5, indicates a constant adsorption Γ over a range of bulk

Figure 5. Interfacial tension as a function of the logarithm of the molar concentration of SOPC determined from the data shown in Figure 4 for different values of $\Delta\phi^{w-o}$. Note that the corresponding values of $\log(C/M)$ for the two concentrations studied by X-ray reflectivity are −5.52 for $C = 3$ μM and −4.9 for $C = 12.5$ μM. For clarity, the tension values for $\Delta\phi^{w-o} = -0.17, -0.07$, and 0.03 V are offset by −3 mN m^{-1}, $\Delta\phi^{w-o} = 0.23$ and 0.28 V are offset by 4 mN m^{-1}, and $\Delta\phi^{w-o} = 0.33$ V is offset by 5 mN m^{-1}. Error bars are smaller than the symbol size. Solid lines are linear fits to the lower concentration portion of the measurements; specifically, points from the lowest five concentrations were used to fit each of the data sets for 0.13 V $\leq \Delta\phi^{w-o} \leq$ 0.33 V, whereas points for $\log(C/M) \leq -5$ were used to fit data sets for the other values of $\Delta\phi^{w-o}$.

concentration for a fixed value of $\Delta\phi^{w-o}$. The deviation from linearity that occurs upon increasing $\log(C/M)$ above a certain value indicates that the critical micelle concentration (CMC) has been exceeded, though the interface remains saturated with SOPC lipids. Linearity between γ and $\log(C/M)$ holds for all values of $\Delta\phi^{w-o}$ for the 3 μM ($\log(C/M) = -5.52$) SOPC sample that will be studied with X-ray reflectivity. The other SOPC concentration studied by X-ray reflectivity, 12.5 μM ($\log(C/M) = -4.9$), is above the CMC.

Table 2 lists the slopes of the lines drawn in Figure 5 and the associated interfacial area per SOPC molecule for the 3 μM

**Table 2. Inverse Interfacial Density (Area per Molecule) of SOPC**[a]

$\Delta\phi^{w-o}$ (V)	slope (mN m^{-1})	area per SOPC (Å^2)
−0.17	5.56 ± 0.12	74 ± 2
−0.07	5.56 ± 0.12	74 ± 2
0.03	5.56 ± 0.12	74 ± 2
0.13	5.87 ± 0.18	70 ± 2
0.18	5.87 ± 0.18	70 ± 2
0.23	5.12 ± 0.29	80 ± 4
0.28	4.83 ± 0.23	85 ± 4
0.33	3.33 ± 0.27	123 ± 10

[a]Calculated from the data in Figure 5 for 3 μM SOPC samples.

SOPC samples. Essentially the same values are valid for the 12.5 μM SOPC samples. Interfacial areas of 70−74 Å^2 per SOPC molecule are measured for $\Delta\phi^{w-o} < 0.2$ V. These are in good agreement with values of 70.1 and 66.5 Å^2 reported for DOPC and DPPC bilayer vesicles, respectively, and the value of 71 Å for DOPC monolayers at the electrified liquid–liquid interface.[76,78]

Table 2 also demonstrates a reduction in interfacial SOPC density for increasing $\Delta\phi^{w-o} > 0.2$ V. This reduction is consistent with the additional current observed in the cyclic voltammogram in Figure 3 for $\Delta\phi^{w-o} > 0.15$ V if, as suggested previously, the neutral SOPC lipids are charged either by protonation or complexation with other cations prior to desorbing from the interface.[13,15,76] A small reduction in the area per SOPC is observed at $\Delta\phi^{w-o} = 0.13$ and 0.18 V, which is consistent with the minimum in interfacial tension observed in Figure 4 for this range of $\Delta\phi^{w-o}$.

3.3. X-ray Reflectivity Data. Figure 6 illustrates X-ray reflectivity data $R(Q_z)$ normalized to the Fresnel reflectivity $R_F(Q_z)$ calculated for a flat, structureless interface[34] from samples with 3 and 12.5 μM SOPC in the DCE phase. X-ray reflectivity probes the electron density variation with depth $\langle\rho(z)\rangle$, which has been averaged over the in-plane ($x-y$) region of the X-ray footprint on the sample interface. The coordinate axis z is perpendicular to the interface. The data exhibit Kiessig fringes in the variation of reflectivity with Q_z, which are analogous to interference fringes generated by reflections from the top and bottom of thin films. The presence of these fringes indicates that the lipid layer has a well-defined electron density profile perpendicular to the interface. Reflectivity measurements for -150 mV $\leq \Delta\phi^{w-o} \leq +130$ mV are nearly indistinguishable, indicating that the electron density profile of the SOPC layer is essentially unaffected over this biologically relevant range of electric potential difference. Larger positive values of $\Delta\phi^{w-o}$ lead to successive variations in the measured reflectivity, as indicated in Figure 6 by the monotonic shift in reflectivity minima and maxima. As discussed below, the
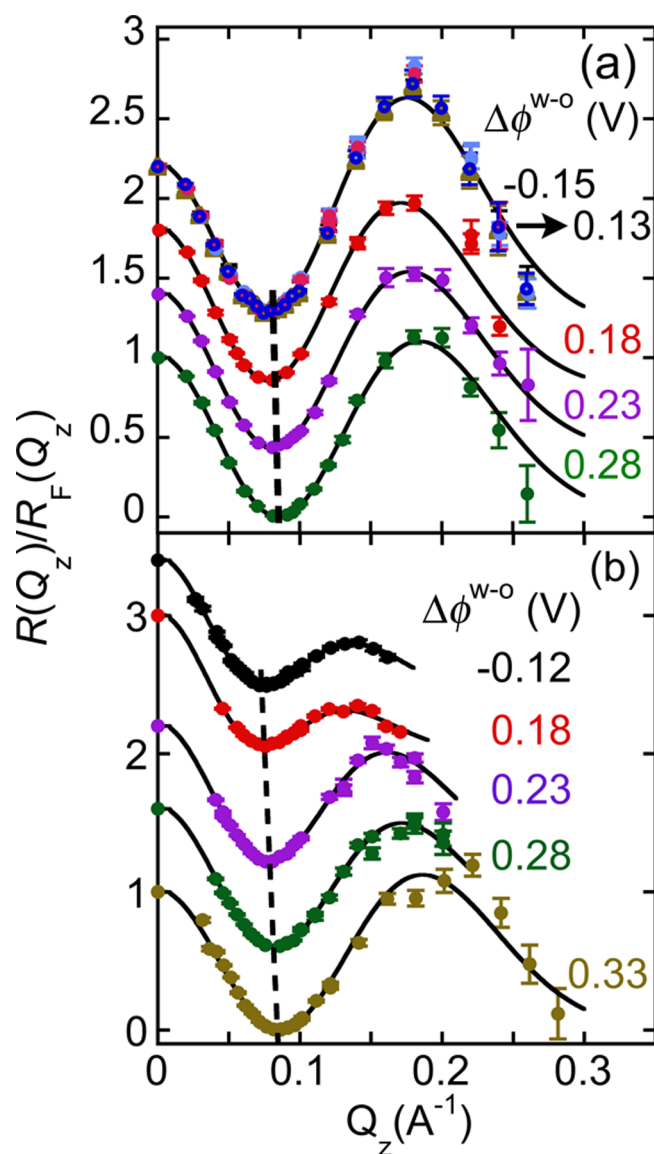
Figure 6. X-ray reflectivity normalized to Fresnel reflectivity $R(Q_z)/R_F(Q_z)$ for various electric potential differences $\Delta\phi^{w-o}$ as a function of wave vector transfer Q_z from liquid−liquid interfaces between (a) 3 μM or (b) 12.5 μM SOPC + 5 mM TDATPBCl in DCE and 0.1 M NaCl + 20 mM HEPES in water. The experiments were carried out at $T \approx 23$ °C. Curves are ordered from top to bottom with increasing $\Delta\phi^{w-o}$ and are successively displaced upward for clarity (note that $R(Q_z)/R_F(Q_z) \rightarrow 1$ as $Q_z \rightarrow 0$ for each separate reflectivity curve). Values at $Q_z = 0$ are measurements of the direct beam when the interface is moved out of the beam path. When $\Delta\phi^{w-o} < 0.18$ V, the reflectivity curves for $\Delta\phi^{w-o} = -0.15, -0.12, -0.07, -0.02, 0.03, 0.08,$ and 0.13 V are indistinguishable, as shown by overlapping data sets for these different values of $\Delta\phi^{w-o}$ in panel a. A similar effect was observed for the 12.5 μM sample whose data is in panel b, but only the −0.12 V data are shown in this case. The two nearly vertical dashed lines follow the variation in position of the first minimum. Fits are described in the text.

qualitative differences in $R(Q_z)/R_F(Q_z)$ for the two different concentrations of SOPC are primarily the result of the smaller interfacial tension of the larger concentration (12.5 μM SOPC) sample, whose larger interfacial roughness influences the X-ray reflectivity.

The data shown in Figure 6 are the result of measurements that span 8 orders of magnitude for each curve, from $R(Q_z) = 1$

to $R(Q_z) \approx 10^{-8}$. Since $R(Q_z)/R_F(Q_z) \sim \exp(-\sigma^2 Q_z^2)$, where σ is the interfacial roughness, the measurable range of Q_z is limited by the roughness, which varies with interfacial tension, as described in section 3.4. For example, the smaller range of Q_z for the reflectivity measured for $\Delta\phi^{w-o} = -0.12$ V in Figure 6b is due to the reduction in reflectivity at larger Q_z that occurs for the large interfacial roughness of ~12 Å. The data sets for the 12.5 μM sample over the range -0.12 V $\leq \Delta\phi^{w-o} \leq 0.23$ V, which were restricted to a smaller range of Q_z, provide limited spatial resolution in the analysis of the SOPC layer structure and will not be used for quantitative analysis of the electron density profile. Extending the range of Q_z beyond that shown was generally not possible because the additional time required for the measurement would have produced radiation damage.

Careful monitoring and reproduction of the data in Figure 6 ensured that radiation damage of the samples was negligible. Several methods were used, including constant checks that data at a given value of Q_z for the same sample were repeatable, data reproducibility between different samples, and repeatability of data measured under conditions of different incident flux on the interface. Although X-ray reflectivity measurements from the liquid−liquid interface are more time-consuming than those from the liquid−vapor interface, the X-ray absorption of the top liquid phase greatly reduces the incident flux on the interface and, consequently, the likelihood of radiation damage.

3.4. X-ray Data Analysis. X-ray reflectivity data are fit to determine the electron density profile and, consequently, the arrangement of SOPC lipid molecules at the interface. A one-slab model that describes the interface as a single slab of thickness L and homogeneous electron density sandwiched between the bulk aqueous and DCE electrolyte solutions could not fit the data in Figure 6. A two-slab model provided a good fit to all the data. As described below, this model provides a sensible correspondence between each slab and the SOPC headgroups or tailgroups.

It is well-known that the applied electric potential difference $\Delta\phi^{w-o}$ establishes an interfacial ion distribution consisting of supporting electrolytes.[79] Therefore, it is to be expected that in addition to the monolayer of lipid molecules at the interface there is a distribution of ions on either side of the lipid layer, which decays from a value near the lipid layer to the bulk ion concentration. Approximately matched X-ray contrast of the ions and solvents produced an ion distribution that has a negligible effect on the interfacial electron density profile. This was confirmed by X-ray reflectivity measurements from samples containing only the electrolyte solutions, i.e., without lipids. These X-ray reflectivity data, measured for $0 \leq \Delta\phi^{w-o} \leq 0.33$ V, could be fit with a simple interface consisting of a step function intrinsic electron density profile roughened by capillary waves,[34] thus demonstrating the essentially negligible effect of the chosen supporting electrolytes on the electron density probed by X-ray reflectivity measurements.[80] The negligible effect of the supporting electrolytes allowed us to fit the X-ray reflectivity data with an interfacial model that consisted of only the lipid monolayer.

A two-slab model of the electron density profile $\langle\rho(z)\rangle$ contains the sum of three error functions (erf), each of which models the variation of electron density through an internal interface (water/headgroup, headgroup/tailgroup, and tailgroup/DCE) within the DCE/SOPC-monolayer/water interfacial structure,

Table 3. Parameters for Two-Slab Model Fitting to X-ray Reflectivity Measurements[a]

SOPC concentration (μM)	$\Delta\phi^{w-o}$ (V)	L_h (Å)	ρ_h (e⁻ Å⁻³)	L_t (Å)	L_{tmin} (Å)	ρ_t (e⁻ Å⁻³)	σ (Å)	L (Å)
3	−0.12	$6.1^{\pm1.4}$	$0.411^{\pm0.037}$	$16^{\pm3}$	12.5	$0.321^{\pm0.009}$	$7.48^{+0.07/-0.58}$	$22.1^{\pm2.6}$
3	0.18	$6.5^{\pm1.5}$	$0.415^{\pm0.039}$	$16^{\pm3}$	13.2	$0.323^{\pm0.011}$	$7.8^{+0.1/-0.6}$	$22.5^{\pm3.1}$
3	0.23	$8.8^{\pm2.4}$	$0.402^{\pm0.029}$	$16^{\pm4}$	11.2	$0.339^{\pm0.012}$	$7.12^{+0.05/-0.56}$	$24.8^{\pm2.4}$
3	0.28	$8.6^{\pm2.3}$	$0.399^{\pm0.025}$	$16^{\pm4}$	10.5	$0.341^{\pm0.009}$	$6.61^{+0.03/-0.37}$	$24.6^{\pm1.9}$
12.5	0.28	$9.1^{\pm2.9}$	$0.408^{\pm0.034}$	$15.2^{\pm4.5}$	10.5	$0.334^{\pm0.011}$	$7.7^{+0.07/-0.6}$	$24.3^{\pm2.7}$
12.5	0.33	$8.7^{\pm2.7}$	$0.401^{\pm0.029}$	$15.1^{\pm4.5}$	7.85	$0.337^{\pm0.012}$	$6.84^{+0.06/-0.39}$	$23.7^{\pm2.3}$

[a]Four parameters are fit to the X-ray reflectivity data: electron densities ρ_h and ρ_t of slabs that include the SOPC headgroups and tailgroups plus intercalated solvents, total thickness $L = L_t + L_h$ of the SOPC monolayer, and thickness L_t of the lipid tailgroup slab. Large error bars on the thickness parameters result from correlations between fitting parameters; however, the resultant electron density profile is accurately determined as described in section 4.3. The headgroup slab thickness L_h is calculated from L and L_t. A lower limit $L_{tmin} = 950/A$ is imposed when fitting the SOPC tailgroup layer thickness, which does not affect the fitted values but only influences the "−" error bar. Similarly, $L - L_t = L_h$ is restricted to lie between 5 and 12 Å. A conservative estimate for L_{tmin} is given by the volume occupied by the SOPC tailgroup V_t (ignoring possible solvent intercalated into the tailgroup region) divided by the area per lipid A listed in Table 2. The value of 950 Å² in the expression for L_{tmin} is determined by the known value of the POPC tailgroup volume,[84,85] which has two fewer carbon atoms in each tail than SOPC. The interfacial roughness σ is calculated from capillary wave theory, where the "+" error is due to measured errors on the interfacial tension and the "−" error is due to the possibility of a small interfacial bending rigidity, $\kappa = 1.5\ k_B T$, as described in section 4.2. Fitting parameters for $\Delta\phi^{w-o} < 0.18$ V (−0.15 V, −0.12 V, −0.07 V, −0.02 V, 0.03 V, 0.08 V, 0.13 V) are essentially the same, so the values for $\Delta\phi^{w-o} = -0.12$ V are given as representative values. Samples with 12.5 μM SOPC and $\Delta\phi^{w-o} < 0.28$ V have an interfacial roughness larger than 8 Å, which produces X-ray reflectivity measurements with limited spatial resolution and, consequently, large errors on the fit parameters. Fitting parameters for these values of $\Delta\phi^{w-o}$ are not shown; nevertheless, analysis of these samples yielded parameters that agreed within error bars with those for the 3 μM SOPC sample at the same values of $\Delta\phi^{w-o}$.

$$\langle\rho(z)\rangle = \frac{1}{2}(\rho_h - \rho_w)\,\text{erf}\left(\frac{z}{\sqrt{2}\,\sigma}\right) + \frac{1}{2}(\rho_t - \rho_h)$$
$$\text{erf}\left(\frac{z - L_h}{\sqrt{2}\,\sigma}\right) + \frac{1}{2}(\rho_{DCE} - \rho_t)$$
$$\text{erf}\left(\frac{z - L_h - L_t}{\sqrt{2}\,\sigma}\right) + \frac{1}{2}(\rho_{DCE} + \rho_w) \tag{2}$$

The electron densities in eq 2 represent the average electron density in the interfacial region of SOPC headgroups, ρ_h, and tailgroups, ρ_t, and of the bulk aqueous (water), ρ_w, and DCE, ρ_{DCE}, phases. The thicknesses of the slabs that correspond to the SOPC headgroup and tailgroup regions are represented, respectively, by L_h and L_t. The interfacial roughness σ represents thermal fluctuations of the interface.[34]

X-ray reflectivity is calculated from $\langle\rho(z)\rangle$ by use of the Parratt algorithm for which $\langle\rho(z)\rangle$ is divided into 300 layers along the z-axis (with a layer spacing of 0.2 Å in the interfacial region) to model the continuously varying density.[81] The calculated reflectivity is used to fit the data in Figure 6 by nonlinear least-squares fitting of the parameters ρ_h, ρ_t, L_t, and the total thickness $L = L_t + L_h$. In addition, a small offset in Q_z, on the order of 1×10^{-3} Å⁻¹ or less, is fit to the data to account for a slight misalignment of the reflectometer. The other three parameters in eq 2, ρ_w, ρ_{DCE}, and σ, are calculated.

The bulk electron densities ρ_w and ρ_{DCE} are calculated using $\rho_s + \sum_{i=1}^{4} n_i(N_i - V_i\rho_s)$, where ρ_s represents the electron density of the pure solvent (water or DCE), n_i is the number density of ion i of the supporting electrolytes, and N_i and V_i are the number of electrons and volume of ion i. The electrolytes dissociate into TDA^+, $TPBCl^-$, Na^+, and Cl^- ions, which do not cross the interface to any appreciable extent for the values of $\Delta\phi^{w-o}$ studied, as illustrated by the cyclic voltammogram in Figure 3. The volumes of Na^+ and Cl^-, respectively, 3.82 and 24.82 Å³, are calculated from their spherical diameters: 1.94 Å for Na^+ and 3.60 Å for Cl^-.[82] The volumes of TDA^+ and $TPBCl^-$, respectively 1219.02 and 531.32 Å³, are calculated as solvent excluded volumes within the software Gaussian.[83] This yields the bulk electron densities of the DCE and aqueous phases to be 0.3795 and 0.3344 e⁻ Å⁻³, only slightly different

from the values of 0.3804 e⁻ Å⁻³ for pure DCE and 0.3335 e⁻ Å⁻³ for pure water (at 23 °C). The critical wave vector for total reflection, $Q_c = 0.00795$ Å⁻¹, determined by these densities is consistent with the X-ray reflectivity data.[34]

The interfacial roughness σ is calculated from the measured interfacial tension γ and capillary wave theory, $\sigma^2 = (k_B T/2\pi\gamma)\ln(q_{max}/q_{min})$, where T is the temperature, $q_{max} = 2/r = 2(\pi/A)^{1/2}$ is the cutoff for the smallest wavelength capillary waves that uses r as the effective cross-sectional radius, A is the area per lipid, and q_{min} is the smallest capillary wave vector that can be resolved by the X-ray measurements, given by $q_{min} = (2\pi/\lambda)\Delta\alpha_s \sin\alpha_i$ ($\Delta\alpha_s = l/d = 5.6 \times 10^{-4}$ is the vertical angular acceptance of the detector, where $l = 1.8$ mm is the electronic slit size and $d = 3.19$ m is the distance from the sample center to the CCD detector).[34] Table 3 lists the calculated values of σ and fitting parameters for the best fits of the X-ray reflectivity data shown in Figure 6.

3.5. MD Simulations. Figure 7 illustrates the top half of the simulation cell for one of the systems listed in Table 1. The monolayer resides in the $x-y$ plane. The simulated areas per lipid are chosen from experimental values and fixed by the $x-y$ dimensions of the simulation cell, which remain constant throughout the simulation (see Table 1 for a description of the five different simulation cells). Figure 8 shows the profile of the electric potential difference along the z-axis calculated using the simulated charge density and Poisson's equation for the five systems listed in Table 1.[86] An electric potential difference across the lipid monolayer is present even in the absence of an applied electric field, as illustrated in Figure 8, as a result of, for example, the potential drop across the interfacial region that contains partially oriented headgroup dipoles (represented by the jagged peaks at $z \approx 100$ Å). The potential difference simulated for zero applied electric field $\Delta\phi_{s,0}$ is taken as the reference potential difference to determine the simulated electric potential difference between the water and oil (DCE) phases, $\Delta\phi_s^{w-o} = \Delta\phi_{s,0} - \Delta\phi_s$, where $\Delta\phi_s$ is the simulated electric potential difference for nonzero applied electric field (Figure 8). This reference potential difference is comparable to the experimental reference $\Delta\phi_{pzc}^{w-o}$, discussed in section 2.2, that corresponds to a sample for which the ion distribution $c_i(z)$ is

9326

dx.doi.org/10.1021/jp5098525 | J. Phys. Chem. B 2015, 119, 9319−9334
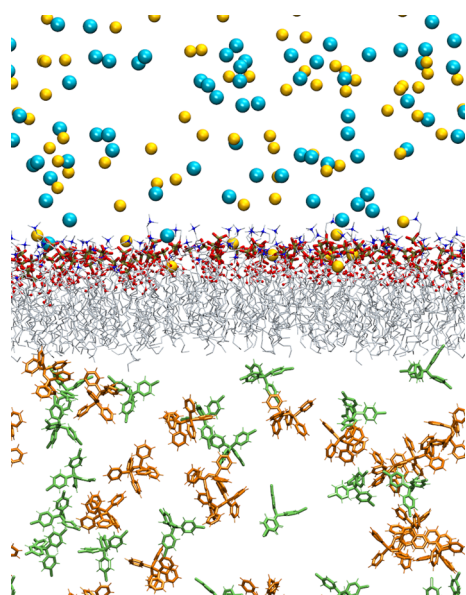
Figure 7. SOPC monolayer at the water (top)−DCE (bottom) interface in the top half of the simulated unit cell. The area per lipid molecule in this snapshot is 121 Å², and a 0.33 V electric potential difference is applied across the monolayer such that the water is at a higher potential. The cations Na⁺ and BTPPA⁺ are colored yellow and brown, respectively, and the anions Cl⁻ and TPBCl⁻ are blue and green, respectively. Within the lipid monolayer, the tailgroups are colored gray, red dots are water molecules within the headgroup region, brown with red bars are phosphate groups, and blue dots with white bars are the $N(CH_3)_3$ groups. Solvents are not shown for clarity.
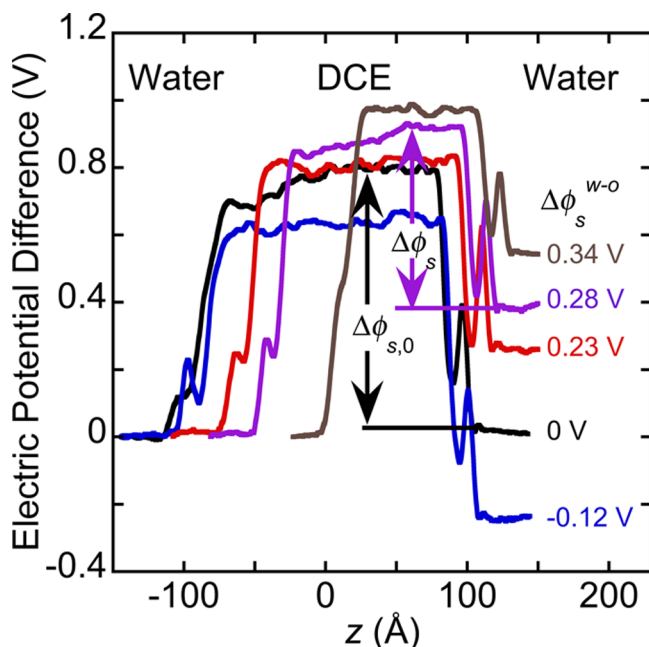
Figure 8. Simulated electric potential difference profiles. The simulation cell consists of water/DCE/water electrolyte solutions with a lipid monolayer at each interface. The simulated electric potential difference between the water and DCE phases (across the SOPC monolayer at $z \approx 100$ Å) in the absence of an applied electric field is shown by $\Delta\phi_{s,0}$. The electric potential difference in the presence of electric fields is shown for one value of $\Delta\phi_s$.

constant as z varies from the interface to the bulk, in the absence of lipids.

The simulated SOPC lipid monolayer is further characterized by calculating its thickness L_s and orientation angles α of the SOPC headgroup and β of the entire SOPC molecule, where the angles are illustrated in Figure 9.[87] The headgroup tilt angle
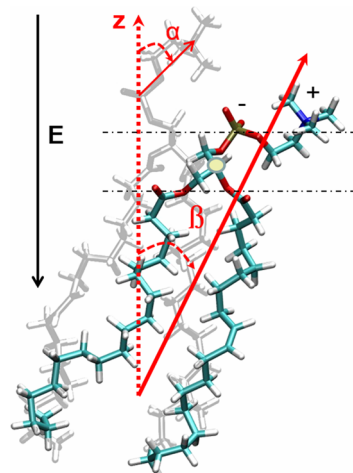
Figure 9. Simulated tilt angles α and β of SOPC. The faded grayscale image illustrates a typical SOPC orientation in zero applied electric field (fixed area per lipid of 72 Å²), and the normal colored image illustrates a typical SOPC orientation in a large electric field ($E = 0.08999$ kcal mol⁻¹ Å⁻¹ e⁻¹ with a fixed area per lipid of 121 Å²). Horizontal dashed lines show the boundaries where a small force (=0.2 kcal/mol/Å) is applied to constrain vertical fluctuations of the C2 carbon (yellow dot) in each lipid.

α is measured between the z-axis and a line connecting P to N atoms in the headgroup. The molecule tilt angle β is measured between the first principle axis of the lipid molecule and the z-axis. Average values of these parameters are calculated by averaging over all 100 lipids in the monolayer and then further averaging over the 500 simulation frames that span the last 4 ns of each simulation trajectory. The thickness L_s is the difference between the maximum and minimum z atomic coordinates of each lipid. Table 4 shows that the membrane thins with increasingly positive electric fields.

Figure 10 illustrates electron density profiles calculated from MD simulations for the five systems. They exhibit a peak of higher electron density corresponding to the interfacial region containing SOPC headgroups and a lower electron density region corresponding to the SOPC tailgroups. The thinning of the lipid monolayer with increasing $\Delta\phi_s^{w-o}$ is clearly observable. A comparison with experimental results will be presented in the Discussion section.

4. DISCUSSION

4.1. Electron Density Profile. X-ray reflectivity measurements of the SOPC monolayer were analyzed in terms of an intrinsic electron density profile roughened by thermal capillary waves, where the two-slab model given in eq 2 with the roughness σ set to zero describes the intrinsic electron density profile. The full experimental electron density profile probed by X-ray reflectivity is given by the two-slab model with the best-fit parameters listed in Table 3, including nonzero roughness σ whose effect is to smear the profile along the z-axis. Neither the full nor the intrinsic electron density profiles can be compared directly to the profile from MD simulations shown in Figure 10 because the small cross-sectional dimensions of the simulation

Table 4. Simulation Results[a]

$\Delta\phi^{w-o}$ (V)	area per lipid (Å²)	L_s (Å)	$L_{s,SOPC}$	α (deg)	β (deg)	N_{H_2O}	N_{DCE}
−0.12	72.25	23.9 ± 0.2	24.9 ± 0.2	66.1 ± 1.6	16.5 ± 1.1	11.1 ± 0.3	4.0 ± 0
0	72.25	23.7 ± 0.2	24.8 ± 0.2	65.7 ± 1.8	17.4 ± 1.2	11.0 ± 0.1	4.0 ± 0
0.23	81.00	23.1 ± 0.2	24.7 ± 0.3	66.5 ± 1.5	20.5 ± 1.4	13.1 ± 0.5	4.7 ± 0.5
0	81.00	23.3 ± 0.1	24.7 ± 0.2	65.6 ± 1.4	19.5 ± 1.1	13.1 ± 0.3	4.9 ± 0.3
0.28	90.25	22.3 ± 0.2	24.7 ± 0.4	68.3 ± 1.4	25.5 ± 2.0	14.6 ± 0.6	5.0 ± 0.2
0	90.25	23.1 ± 0.1	24.8 ± 0.2	65.7 ± 1.7	21.3 ± 0.9	15.5 ± 0.6	5.5 ± 0.5
0.33	121.0	21.3 ± 0.2	24.7 ± 0.4	73.4 ± 2.4	30.3 ± 2.4	19.5 ± 0.9	7.0 ± 0.3
0	121.0	21.8 ± 0.2	24.9 ± 0.3	68.7 ± 2.0	28.9 ± 1.0	21.5 ± 0.6	7.8 ± 0.4

[a]L_s represents the simulated thickness of the lipid monolayer, the calculated value $L_{s,SOPC} = L_s/\cos\beta$ is the total length of SOPC molecules calculated from the simulated L_s and β, where the angles α and β denote the tilt angles of the SOPC headgroup and the entire SOPC molecule measured from the z-axis (Figure 9), N_{H_2O} is the number of water molecules per lipid within the headgroup region, and N_{DCE} is the number of DCE molecules per lipid in the tailgroup region. The multiple simulations for $\Delta\phi^{w-o} = 0$ V for different areas per lipid will be discussed in section 4.4.
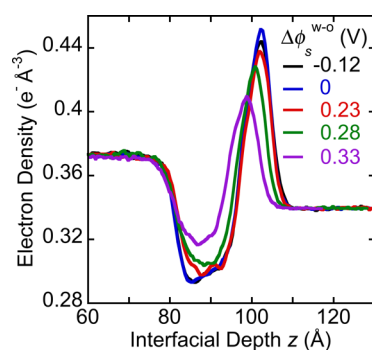

Figure 10. Electron density profiles calculated from MD simulations for different values of $\Delta\phi_s^{w-o}$.

cell (e.g., 85 × 85 Å²) limit the capillary wave roughness to a small but nonzero value, 3.2 Å, whereas the experimental value of roughness is close to 7 Å.

Figure 11 illustrates a comparison between the full experimental electron density profiles and MD simulated electron density profiles that have been modified by fitting the simulated profiles with the two-slab model and then roughening them using values of σ from experiment (Table 3). This procedure allows for the comparison of equally roughened profiles from experiment and simulation. Importantly, this comparison uses electron density profiles that are determined directly from experiment. The two sets of profiles are qualitatively similar, though there are some quantitative differences. The simulated values of total monolayer thickness are slightly larger than experimental values, though the trend toward thinning with increasingly positive electric potential difference is observed in both sets of profiles. The simulated electron density value is smaller in the tailgroup minimum by about 0.01 e⁻ Å⁻³ and larger in the headgroup maximum by a similar amount. Similar discrepancies between experimental and simulated values are present in the electron densities of the bulk DCE and water phases.

4.1.1. Tailgroup Region. Close-packed saturated alkyl chains have electron densities that vary from 0.325 to 0.343 e⁻ Å⁻³ for alkane rotator phases to crystalline bulk phases of long chain alkanols.[88] Such close-packed chains have a cross-sectional area of ∼19 Å² that is much smaller than half the 70 Å² per lipid or greater interfacial area that is occupied by the disordered monolayer of two-tailed SOPC. The unsaturated oleoyl tail of SOPC frustrates the chain packing, forcing it to occupy a larger interfacial area than close-packed chains. Therefore, even though values of the intrinsic electron density ρ_t of the
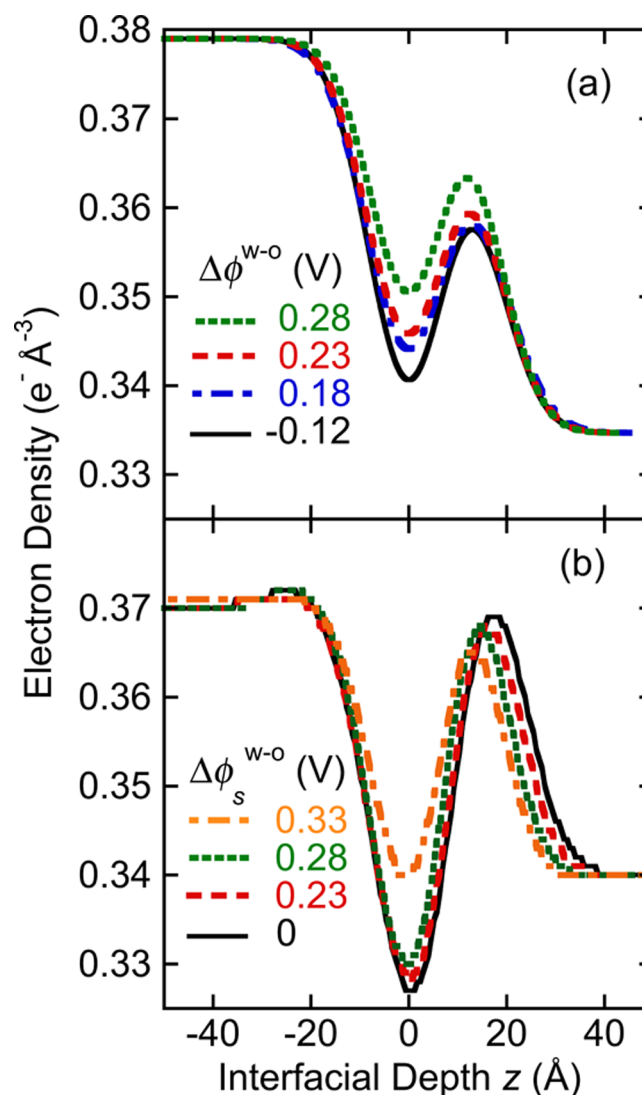
Figure 11. Fitted electron density profiles from (a) X-ray reflectivity of the 3 μM SOPC samples and (b) MD simulations. The curves shown in panel b are the result of fitting the MD simulations in Figure 10 to a two-slab model and then adjusting the value of interfacial roughness to match the experimental value for the corresponding electric potential difference $\Delta\phi^{w-o}$.

tailgroup slab, determined by X-ray reflectivity, vary from 0.32 to 0.34 e⁻ Å⁻³ (Table 3), they cannot represent close-packed

tailgroups. Instead, this electron density is the combination of loosely packed, disordered tailgroups, with an average electron density less than 0.32 e$^-$ Å^{-3}, and DCE molecules, whose bulk phase electron density is 0.38 e$^-$ Å^{-3}, intercalating into the tailgroups. A simple estimate of the number n of DCE molecules per lipid that intercalate into the tailgroup, based upon the number of electrons and volume of the tailgroups and DCE molecules, is provided by $\rho_{tail} = (274 + 50n)/(960 + 131n)$, where 274 is the number of electrons in the two-chained tailgroup $(C_{34}H_{70})$, 50 is the number of electrons in a DCE molecule, 960 Å^3 is an estimate for the volume occupied by the tailgroup chains,[88] and 129 Å^3 is the volume of a DCE molecule determined from the bulk density of DCE. Varying the value of ρ_{tail} over the measured values of $0.32{-}0.34$ e$^-$ Å^{-3} suggests that $4{-}10$ DCE molecules per lipid intercalate into the tailgroup region. This is consistent with the $4{-}8$ DCE molecules observed in the tailgroup region by MD simulations (N_{DCE} in Table 4). As $\Delta\phi^{w-o}$ increases, the area per lipid increases, thus allowing for greater intercalation of the DCE and an increase in the tailgroup electron density. Figure 12 shows that the trend in electron density with $\Delta\phi^{w-o}$ is consistent with MD simulations.
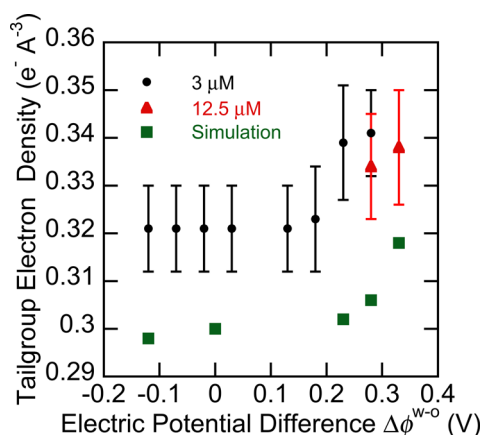

Figure 12. Comparison of the intrinsic electron density of the interfacial tailgroup slab determined by fitting X-ray reflectivity measurements (Table 3) and MD simulations.

The disordered nature of SOPC tailgroups is consistent with the $15{-}16$ Å thickness of the tailgroup slab determined by X-ray reflectivity (Table 3). An all-trans alkyl chain with 17 carbon atoms will have a length of 21.7 Å ($=(17 - 1 + (9/8))$ $\times$ 1.265 Å),[89] significantly longer than the measured thickness of the tailgroup slab.

4.1.2. Headgroup Region. The thickness of the SOPC headgroup region, $6.1{-}9.1$ Å (Table 3), is consistent with literature values that vary from 7 to 12 Å for PC lipid headgroup thickness in monolayers on liquid surfaces.[90] Similarly, the measured headgroup electron density of $0.399{-}0.415$ e$^-$ Å^{-3} lies within the range of values previously observed.[90] Note that measurements of the volume of the PC headgroup of $\sim$320 Å^3 yield a bare headgroup electron density of 0.53 e$^-$ Å^{-3}.[84,85,91] Substantial hydration of the headgroup is required to reduce its bare electron density to the measured values. A simple estimate, based upon the number of electrons and volume of the headgroups and water molecules, suggests that $15{-}20$ water molecules per lipid hydrate the headgroup region, respectively, when the headgroup electron density varies from 0.415 to 0.399 e$^-$ Å^{-3} (Table 3). This is fairly consistent

with the $11{-}21$ water molecules in the headgroup layer observed by MD simulations (Table 4). Both experiments and simulations are consistent with an increase in headgroup water with area per lipid. However, closer observation of the simulations reveals that only five of the water molecules are hydrogen-bonded to the headgroup (Figure 13), a number that
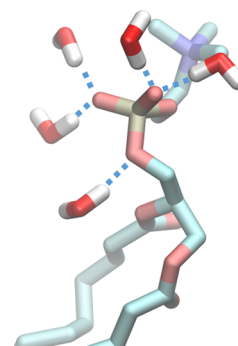
Figure 13. MD simulation snapshot of hydrogen-bonded water molecules in the SOPC headgroup region.

remains constant for all areas per lipid. Both non-H-bonded and H-bonded water molecules are present at all areas per lipid; however, as the area per lipid increases, additional nonbonded water molecules move into the headgroup region to fill the available space (Figure 14).

4.2. Bending Rigidity. The fluctuation spectrum of lamellar lipid bilayer phases is known to be influenced by the bending rigidity (or modulus) κ.[92] Similarly, the roughness σ of an interface is influenced by κ, which preferentially suppresses short wavelength thermal fluctuations of the interface, as

0.00 V ; 72.25 Å^2 0.23 V ; 81.0 Å^2

0.28 V ; 90.25 Å^2 0.33 V ; 121.0 Å^2
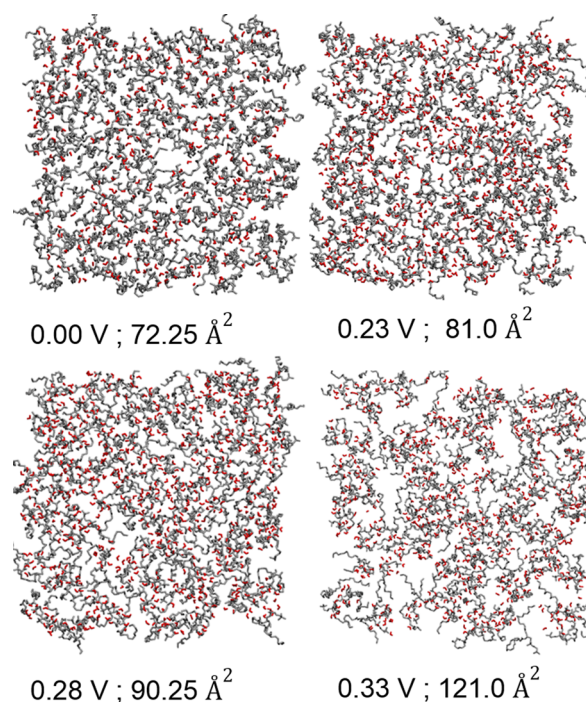
Figure 14. Top view snapshots of SOPC monolayer simulations showing only H-bonded water in red and SOPC molecules in gray for just the top monolayer in the simulation cell. These snapshots illustrate the space available for non-H-bonded water molecules and DCE molecules to intercalate into the monolayer.

observed from the expression for the energy $u(\vec{q}_{xy})$ per capillary mode with wave vector $\vec{q}_{xy}$,[34]

$$u(\vec{q}_{xy}) \approx \frac{|h(\vec{q}_{xy})|^2}{2A_{tot}}[\Delta\rho_m g + \gamma|\vec{q}_{xy}|^2 + \kappa|\vec{q}_{xy}|^4 + ...] \quad (3)$$

where $h(\vec{q}_{xy})$ is the Fourier transform of the surface height function, A_{tot} is the total surface area, $\Delta\rho_m$ is the mass density difference between the two phases, and g is the gravitational acceleration. The surface bending rigidity κ is the amplitude of the $|\vec{q}_{xy}|^4$ term, which is large at short wavelength (i.e., large $|\vec{q}_{xy}|$) capillary waves. The expression in eq 3 leads to a revised expression for the interfacial roughness σ[93]

$$\sigma^2 \approx \frac{k_B T}{2\pi\gamma} \ln \frac{(\gamma/\kappa)^{1/2}}{q_{min}} \quad (4)$$

where the value of q_{min} was given in section 3.4. X-ray reflectivity measurements probe the spatially averaged (over the x–y plane of the interface) fluctuation spectrum to yield the interfacial roughness σ but cannot separate the effect of interfacial tension γ and surface bending rigidity κ on the roughness. Our QELS measurements also probe the thermal fluctuation spectrum but do so at much longer capillary wavelengths (8.5×10^{-5} m for measurements of the third order peak scattered from the grating), thus allowing for a measurement of γ that is unaffected by small values of κ. The analysis of X-ray reflectivity presented in section 3.4 used the value of roughness $\sigma^2 = (k_B T/2\pi\gamma) \ln(q_{max}/q_{min})$ calculated from the QELS measurement of γ. Reanalysis of X-ray reflectivity data with the smaller roughness given by eq 4 can place an upper limit on values of κ that are consistent with the data. Since the surface bending rigidity will have a greater effect on interfaces with low interfacial tension, reanalysis of the 12.5 μM SOPC sample provides the highest accuracy determination of κ within our set of data. In addition, κ is maximized at the highest interfacial density of lipids;[94] therefore, reanalysis of the X-ray reflectivity data from the 12.5 μM SOPC sample at $\Delta\phi^{w-o} = -0.12$ V is used. These data provide an upper limit of $\kappa \leq 1.5\ k_B T$. Under these conditions, the interfacial roughness σ decreases from a value of 12 Å when $\kappa = 0$ to 10.5 Å when $\kappa = 1.5\ k_B T$.

4.3. Total Monolayer Thickness. The values of monolayer thickness L determined from X-ray measurements (listed in Table 3) and values of L_s from MD simulations (listed in Table 4) are very similar, ~22–25 Å, depending on the interfacial area per lipid. These values are comparable to the thickness of SOPC or mixed SOPC:SOPS monolayers previously studied at the water–vapor interface.[38,39,43] The relatively large standard deviations on the X-ray fitting parameters and the possibility of a bending rigidity complicate the detailed comparison of these values, in particular, their variation with $\Delta\phi^{w-o}$. As shown in Table 3, the fitted values of L have one standard deviation errors up to ±3 Å; nevertheless, the electron density profiles that are produced by sets of fit parameters that vary within one standard deviation of the best-fit parameters are visually indistinguishable from the best-fit electron density profiles shown in Figure 11. This shows that the electron density profile is accurately determined by X-ray measurements but that correlations among the fitting parameters yield unphysically large variations. This complication is exacerbated by the inability to directly measure the bending rigidity described in the previous section. Varying the bending rigidity over its range

of possible values (0–$1.5\ k_B T$) yields an additional variation of ~3 Å in the fitting parameter L; however, this does not change the electron density profile. These complications can be circumvented by directly analyzing the electron density profiles.

Figure 15 shows the 10–90 thickness of the SOPC monolayer, calculated by analysis of the electron density
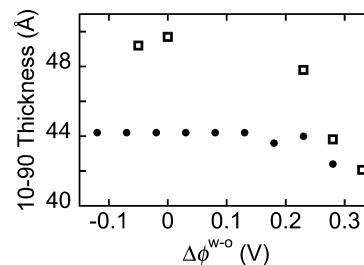
Figure 15. 10–90 monolayer thickness determined by analysis of the electron density profiles shown in Figure 11 from X-ray reflectivity (3 μM SOPC sample, dots) and MD simulations (squares).

profiles in Figure 11a to determine the largest distance between positions z where the density is less than the DCE bulk phase density by 10 and 90% of the density difference between the two bulk phases. Although this measure of monolayer thickness includes the effect of thermal roughness and is substantially larger than the intrinsic monolayer thickness of ~22–25 Å listed in Tables 3 and 4, its advantage is that it allows for a direct comparison of the results of X-ray reflectivity measurements and MD simulations without the complication of correlations in the X-ray fitting parameters. Figure 15 demonstrates that the 10–90 thicknesses are up to 5 Å larger for the simulations, as is confirmed by visual observation of the two panels in Figure 11. Also observable from both experiment and simulation is the thinning of the monolayer at about the same values of $\Delta\phi^{w-o}$, although a larger effect is observed in the simulations.

4.4. Role of the Electric Field. Interfacial tension and X-ray reflectivity measurements of the SOPC monolayer are essentially constant over a biologically relevant range of electric potential differences, -150 mV $\leq \Delta\phi^{w-o} \leq +130$ mV, indicating that the structure of the SOPC layer is unchanged over this range of $\Delta\phi^{w-o}$. MD simulations also show a similar structure at two values of electric potential within this range, -120 mV and 0.0 V, calculated for the ~72 Å^2 area per lipid determined by our experiments. Recent neutron reflectivity measurements of a bilayer of POPC lipids that contained one leaflet (monolayer) tethered to a solid support and the other leaflet physisorbed on top reported a 2 Å thinning of the physisorbed leaflet when the transbilayer voltage was changed from 0 to 100 mV.[53] The neutron measurements displayed a peak in $R(Q_z)/R_F(Q_z)$ but could not observe a full oscillation because of the smaller measured range in Q_z (≤ 0.15 Å^{-1}). Our X-ray reflectivity data shown in Figure 6a and the variations in the measured electron density profile shown in Figure 11a are indistinguishable over the range of potential from -150 to $+130$ mV and are not consistent with a change of 2 Å in, for example, the 10–90 thickness of the monolayer, within a statistical accuracy of at least four standard deviations. Fitting parameter variations that led to a change of 2 Å in the 10–90 thickness of the monolayer over this range of potentials would produce a poor fit to the X-ray reflectivity data.

Measurements at higher positive potentials, from 180 to 330 mV, illustrate a monotonic increase in the interfacial area per lipid and accompanying variations in the interfacial ordering of the lipid. MD simulations of the headgroup angle α show little change until it increases at the highest potential differences of 280 mV (90.25 Å^2) and 330 mV (121 Å^2), yet the molecule angle β has changed substantially by 230 mV (81 Å^2) and has an overall larger increase than α up to potentials of 330 mV (121 Å^2); see Table 4. If SOPC rotated as a rigid body, then increased values of β should lead to similar increases in α. It seems that the headgroup interactions, possibly with the aqueous phase or with neighboring headgroups, have a stabilizing effect on the headgroup orientation. Nevertheless, constancy of the length along the first principle axis of the SOPC, shown by values of $L_{s,OPC} = Ls/\cos \beta$ listed in Table 4, indicates that the variation in membrane thickness is due primarily to nearly rigid-body rotation of the entire SOPC molecule and only secondarily to changes in the molecular configuration.

It is interesting to ask if the changes in the structure of the lipid monolayer with electric potential difference are due to rotation of the headgroup dipole by the electric field or to some other mechanism. The approximate energy of a headgroup dipole in an electric field, $U = -\vec{p}\cdot\vec{E}$, is calculated to be ~0.1 k_BT for a headgroup dipole moment of 10 D and electric field amplitudes of ~10^7 V m^{-1}, which are similar to those used in the simulations (Table 1).[95] Although the effective headgroup dipole moment can be varied by complexing with water or other lipids, the conclusion of small dipole energies should apply to our single-component monolayers.[4,95,96] In addition, if electric dipole interactions were the dominant source of the observed changes, then we would have expected changes in the headgroup angle α to lead changes in β as a result of the torque on the headgroup dipole. Instead, MD simulations show the opposite; changes in α lag those in β.

Alternatively, the changes in lipid monolayer structure could be due to the larger area per lipid that is due to something else besides the electric field torque on the headgroup. Several authors have suggested that the increased interfacial tension observed at higher $\Delta\phi^{w-o}$ as well as electrochemical observations of increased current in the cyclic voltammogram at similar values of $\Delta\phi^{w-o}$ are the result of a decreased interfacial density of lipids.[13,14,16,17] They proposed a chemical mechanism in which interfacial PC lipids become positively charged by proton or cation binding at an appropriate positive value of $\Delta\phi^{w-o}$ and are subsequently desorbed from the interface into the bulk organic phase.[13,14] Although our X-ray experiments and MD simulations did not directly test this chemical mechanism, our MD simulations show that most of the observed structural effects are due to variations in lipid interfacial density and not to the applied electric field. Note that the MD simulations did not try to mimic this chemical mechanism but fixed the number of lipid molecules in the layer. Nevertheless, the MD simulations can independently vary the area per lipid and the applied electric field. Simulations at $\Delta\phi^{w-o} = 0$ for different interfacial areas per lipid produced similar values for the monolayer thickness and tilt angles as did the corresponding simulations at the same areas per lipid but at values of $\Delta\phi^{w-o}$ that mimic the experiments (Table 4). Only at the two highest values of area per lipid, 90 and 121 Å^2, are differences observed in the monolayer structure between simulations at 0 V and the two corresponding highest values of potential difference, 280 and 330 mV. It appears that there is

some influence of the electric field interaction with the lipid dipole on lipid ordering at the highest values of $\Delta\phi_s^{w-o}$, but the primary determinant of lipid ordering is the interfacial area per lipid.

5. CONCLUSIONS

The effect of membrane potential on the molecular ordering of lipids within a biomimetic membrane—a self-assembled monolayer of SOPC lipids at a liquid–liquid interface between two immiscible electrolyte solutions—was studied with X-ray reflectivity and interfacial tension measurements, as well as MD simulations. Interfacial tension and X-ray reflectivity measurements demonstrate that stable and reproducible SOPC monolayers are formed with interfacial densities that can be varied from values typical of unsaturated lipids in biomimetic systems (~70 Å^2 per lipid molecule) to densities lower by about a factor of 2. Measurements of the high density SOPC monolayers are nearly indistinguishable over a biologically relevant range of electric potential differences, -150 mV $\leq \Delta\phi^{w-o} \leq +130$ mV, indicating that the molecular order within the SOPC layer is unchanged over this range of $\Delta\phi^{w-o}$. Measurements at higher positive potentials, up to 330 mV, illustrate a monotonic increase in the interfacial area per lipid and accompanying variations in the interfacial ordering of the lipid.

X-ray reflectivity measurements determined values of the thickness and electron densities of the two interfacial regions containing SOPC headgroups and tailgroups. These values demonstrated that solvent must intercalate into the SOPC layer, specifically water hydration of the headgroup and DCE solvation of the tailgroup. Upon accounting for this intercalation, the structure of the SOPC layer is consistent with values in the literature for layers of unsaturated lipids in other geometries, such as bilayer vesicles or Langmuir monolayers. In addition, the predictions of MD simulations for the number of hydration water molecules and intercalated DCE molecules are in quantitative agreement with the measured electron densities. Ion penetration into the lipid headgroup region is small in the MD simulations and not observable in the X-ray reflectivity measurements. The variation in total monolayer thickness with electric potential difference $\Delta\phi^{w-o}$ determined by X-ray reflectivity is consistent with the MD simulations, with small quantitative differences between them. Finally, a combination of X-ray reflectivity and quasi-elastic light scattering measurements placed a small upper limit on the interfacial bending rigidity, $\kappa \leq 1.5\ k_BT$, of the monolayer.

The close correspondence between the structure of the monolayer predicted by MD simulations and measured by X-ray reflectivity over the experimental values of $\Delta\phi^{w-o}$ provides a justification to use the simulation results to address whether the change in monolayer structure with $\Delta\phi^{w-o}$ is due to the torque on the dipole moment of the PC lipid headgroup or to some other influence of $\Delta\phi^{w-o}$ that leads to an increase in interfacial area per lipid. Simulations show that the lipid molecular ordering is determined primarily by changes in interfacial area per lipid, and only secondarily to the electrostatic interaction of the dipole moment with the electric field. These results provide indirect support for a previously published proposal that protonation or cation binding to the lipid, which takes place at an appropriate positive value of the potential difference $\Delta\phi^{w-o}$, leads to a loss of lipid from the

interface and, consequently, to an increase in area per lipid at higher values of $\Delta\phi^{w-o}$.[13,14,17]

■ AUTHOR INFORMATION

Corresponding Author

*E-mail: schloss@uic.edu.

Notes

The authors declare no competing financial interest.

■ REFERENCES

(1) Lippe, G.; Sorgato, M. C.; Harris, D. A. The Binding and Release of the Inhibitor Protein Are Governed Independently by ATP and Membrane Potential in Ox-Heart Submitochondrial Vesicles. *Biochim. Biophys. Acta, Bioenerg.* **1988**, *933*, 12−21.

(2) Dimroth, P.; Kaim, G.; Matthey, U. Crucial Role of the Membrane Potential for ATP Synthesis by F1Fo ATP Synthases. *J. Exp. Biol.* **2000**, *203*, 51−59.

(3) Armstrong, C. M.; Hille, B. Voltage-Gated Ion Channels and Electrical Excitability. *Neuron* **1998**, *20*, 371−380.

(4) Radhakrishnan, A.; McConnell, H. M. Electric Field Effect on Cholesterol-Phospholipid Complexes. *Proc. Natl. Acad. Sci. U.S.A.* **2000**, *97*, 1073−1078.

(5) Neumann, E.; Rosenheck, K. Permeability Changes Induced by Electric Impulses in Vesicular Membranes. *J. Membr. Biol.* **1972**, *10*, 279−290.

(6) Kinosita, K., Jr.; Tsong, T. Y. Formation and Resealing of Pores of Controlled Sizes in Human Erythrocyte Membrane. *Nature* **1977**, *268*, 438−441.

(7) Vanysek, P.; Ruth, W.; Koryta, J. Valinomycin Mediated Transfer of Potassium across the Water/Nitrobenzene Interface. A Study by Voltammetry at the Interface between Two Immiscible Electrolyte Solutions. *J. Electroanal. Chem.* **1983**, *148*, 117.

(8) Girault, H. H.; Schiffrin, D. J. Charge Effects on Phospholipid Monolayers in Relation to Cell Motility. *Biochim. Biophys. Acta* **1986**, *857*, 251−258.

(9) Volkov, A. G. *Liquid Interfaces in Chemical, Biological, and Pharmaceutical Applications*; Marcel Dekker: New York, 2001.

(10) Malkia, A.; Liljeroth, P.; Kontturi, K. Membrane Activity of Ionisable Drugs - a Task for Liquid-Liquid Electrochemistry? *Electrochem. Commun.* **2003**, *5*, 473.

(11) Maeda, K.; Yoshida, Y.; Goto, T.; Marecek, V. Blocking Effect of a Phospholipid Monolayer on Ion Transfer at a Liquid/Liquid Interface and Its Electrochemical Control. *J. Electroanal. Chem.* **2004**, *567*, 317.

(12) Nagatani, H.; Samec, Z.; Brevet, P.-F.; Fermin, D. J.; Girault, H. H. Adsorption and Aggregation of Meso-Tetrakis(4-Carboxyphenyl)-Porphyrinato Zinc(II) at the Polarized Water|1,2-Dichloroethane Interface. *J. Phys. Chem. B* **2003**, *107*, 786.

(13) Marecek, V.; Lhotsky, A.; Janchenova, H. Mechanism of Lecithin Adsorption at a Liquid/Iquid Interface. *J. Phys. Chem. B* **2003**, *107*, 4573−4578.

(14) Samec, Z.; Trojanek, A.; Girault, H. H. Thermodynamic Analysis of the Cation Binding to a Phosphatidylcholine Monolayer at a Polarised Interface between Two Immiscible Electrolyte Solutions. *Electrochem. Commun.* **2003**, *5*, 98−103.

(15) Samec, Z.; Trojanek, A.; Krtil, P. Dynamics of Phospholipid Monolayers on Polarised Liquid-Liquid Interfaces. *Faraday Discuss.* **2005**, *129*, 301.

(16) Grandell, D.; Murtomaki, L.; Kontturi, K.; Sundholm, G. Phospholipid Monolayers Studied by a Combination of Cyclic Voltammetry and Langmuir Techniques at the Water 1,2-Dichloroethane Interface. *J. Electroanal. Chem.* **1999**, *463*, 242−247.

(17) Kakiuchi, T.; Nakanishi, M.; Senda, M. The Electrocapillary Curves of the Phosphatidylcholine Monolayer at the Polarized Oil-Water Interface. II. Double Layer Structure of Dilauroylphosphatidylcholine Monolayer at the Nitrobenzene-Water Interface. *J. Electroanal. Chem.* **1989**, *62*, 403−409.

(18) Miller, I. R.; Bach, D. Structure and Membrance Properties of Lecithin Monolayers at the Polarized Mercury/Water Interface. *J. Colloid Interface Sci.* **1969**, *29*, 250−260.

(19) Bizzotto, D.; Yang, Y. G.; Shepherd, J. L.; Stoodley, R.; Agak, J.; Stauffer, V.; Lathuilliere, M.; Akhtar, A. S.; Chung, E. Electrochemical and Spectroelectrochemical Characterization of Lipid Organization in an Electric Field. *J. Electroanal. Chem.* **2004**, *574*, 167−184.

(20) Vakurov, A.; Galluzzi, M.; Podesta, A.; Gamper, N.; Nelson, A. L.; Connell, S. D. A. Direct Characterization of Fluid Lipid Assemblies on Mercury in Electric Fields. *ACS Nano* **2014**, *8*, 3242−3250.

(21) Brukhno, A. V.; Akinshina, A.; Coldrick, Z.; Nelson, A.; Auer, S. Phase Phenomena in Supported Lipid Films under Varying Electric Potential. *Soft Matter* **2011**, *7*, 1006−1017.

(22) Sachs, J. N.; Crozier, P. S.; Woolf, T. B. Atomistic Simulations of Biologically Realistic Transmembrane Potential Gradients. *J. Chem. Phys.* **2004**, *121*, 10847−10851.

(23) Suenaga, A.; Komeiji, Y.; Uebayasi, M.; Meguro, T.; Saito, M.; Yamato, I. Computational Observation of an Ion Permeation through a Channel Protein. *Biosci. Rep.* **1998**, *18*, 39−48.

(24) Gurtovenko, A. A.; Vattulainen, I. Pore Formation Coupled to Ion Transport through Lipid Membranes as Induced by Transmembrane Ionic Charge Imbalance: Atomistic Molecular Dynamics Study. *J. Am. Chem. Soc.* **2005**, *127*, 17570−17571.

(25) Khalili-Araghi, F.; Tajkhorshid, E.; Schulten, K. Dynamics of K1 Ion Conduction through Kv1.2. *Biophys. J.* **2006**, *91*, L72−L74.

(26) Gurtovenko, A. A.; Vattulainen, l. Ion Leakage through Transient Water Pores in Protein-Free Lipid Membranes Driven by Transmembrane Ionic Charge Imbalance. *Biophys. J.* **2007**, *92*, 1878−1890.

(27) Denning, E. J.; Crozier, P. S.; Sachs, J. N.; Woolf, T. B. From the Gating Charge Response to Pore Domain Movement: Initial Motions of Kv1.2 Dynamics under Physiological Voltage Changes. *Mol. Membr. Biol.* **2009**, *26*, 397−421.

(28) Khalili-Araghi, F.; Jogini, V.; Yarov-Yarovoy, V.; Tajkhorshid, E.; Roux, B.; Schulten, K. Calculation of the Gating Charge for the Kv1.2 Voltage-Activated Potassium Channel. *Biophys. J.* **2010**, *98*, 2189−2198.

(29) Zhonga, Q.; Husslein, T.; Moore, P. B.; Newns, D. M.; Pattnaik, P.; Klein, M. L. The M2 Channel of Influenza a Virus: A Molecular Dynamics Study. *FEBS Lett.* **1998**, *434*, 265−271.

(30) Tieleman, D. P.; Berendsen, H. J. C.; Sansom, M. S. P. Voltage-Dependent Insertion of Alamethicin at Phospholipidwater and Octane/Water Interfaces. *Biophys. J.* **2001**, *80*, 331.

(31) Tieleman, D. P. The Molecular Basis of Electroporation. *BMC Biochem.* **2004**, *5*, 10.

(32) Tieleman, D. P.; Leontiadou, H.; Mark, A. E.; Marrink, S. J. Simulation of Pore Formation in Lipid Bilayers by Mechanical Stress and Electric Fields. *J. Am. Chem. Soc.* **2003**, *125*, 6382−6383.

(33) Tarek, M. Membrane Electroporation: A Molecular Dynamics Simulation. *Biophys. J.* **2005**, *88*, 4045−4053.

(34) Pershan, P. S.; Schlossman, M. L. *Liquid Surfaces and Interfaces: Synchrotron X-Ray Methods*; Cambridge University Press: Cambridge, U.K., 2012.

(35) Als-Nielsen, J.; Kjaer, K. X-Ray Reflectivity and Diffraction Studies of Liquid Surfaces and Surfactant Monolayers. In *Phase Transitions in Soft Condensed Matter*; Riste, T., Sherrington, D., Eds.; Plenum Press: New York, 1989; Vol. *211*, p 145.

(36) Mohwald, H. Phospholipid and Phospholipid-Protein Monolayers at the Air/Water Interface. *Annu. Rev. Phys. Chem.* **1990**, *41*, 441.

(37) Losche, M. Surface-Sensitive X-Ray and Neutron Scattering Characterization of Planar Lipid Model Membranes and Lipid/Peptide Interactions. *Curr. Top. Membr.* **2002**, *52*, 117−161.

(38) Malkova, S.; Long, F.; Stahelin, R. V.; Pingali, S. V.; Murray, D.; Cho, W.; Schlossman, M. L. X-Ray Reflectivity Studies of cPLA$_2\alpha$-C2 Domains Adsorbed onto Langmuir Monolayers of Sopc. *Biophys. J.* **2005**, *89*, 1861−1873.

(39) Chen, C.-H.; Malkova, S.; Pingali, S. V.; Long, F.; Garde, S.; Cho, W.; Schlossman, M. Configuration of PKCα-C2 Domain Bound to Mixed SOPC/SOPS Lipid Monolayers. *Biophys. J.* **2009**, *97*, 2794−2802.

(40) Krishnan, V.; Strzalka, J.; Liu, J.; Liu, C. A.; Kuzmenko, I.; Gog, T.; Blasie, J. K. Interferometric Enhancement of X-Ray Reflectivity from Unperturbed Langmuir Monolayers of Amphiphiles at the Liquid-Gas Interface. *Phys. Rev. E* **2010**, *81*, 021604-1−021604-10.

(41) Wang, W.; Bu, W.; Wang, L.; Palo, P. E.; Mallapragada, S.; Nilsen-Hamilton, M.; Vaknin, D. Interfacial Properties and Iron Binding to Bacterial Proteins That Promote the Growth of Magnetite Nanocrystals: X-Ray Reflectivity and Surface Spectroscopy Studies. *Langmuir* **2012**, *28*, 4274−4282.

(42) Akgun, B.; Satija, S.; Nanda, H.; Pirrone, G. F.; Shi, X.; Engen, J. R.; Kent, M. S. Conformational Transition of Membrane-Associated Terminally Acylated HIV-1 Nef. *Structure* **2013**, *21*, 1822−1833.

(43) Tietjen, G. T.; Gong, Z.; Chen, C.-h.; Vargas, E.; Crooks, J. E.; Cao, K.; Heffern, C. T. R.; Henderson, J. M.; Meron, M.; Lin, B. Molecular Mechanism for Differential Recognition of Membrane Phosphatidylserine by the Immune Regulatory Receptor Tim4. *Proc. Natl. Acad. Sci. U.S.A.* **2014**, *111*, E1463−E1472.

(44) Zhang, Z.; Mitrinovic, D. M.; Williams, S. M.; Huang, Z.; Schlossman, M. L. X-Ray Scattering from Monolayers of F-(CF$_2$)$_{10}$(CH$_2$)$_2$OH at the Water-(Hexane Solution) and Water-Vapor Interfaces. *J. Chem. Phys.* **1999**, *110*, 7421−7432.

(45) Schlossman, M. L.; Mitrinovic, D. M.; Zhang, Z.; Li, M.; Huang, Z. X-Ray Scattering from Single Liquid-Liquid Interfaces. *Synchrotron Radiat. News* **1999**, *12*, 53−58.

(46) Tikhonov, A. M.; Pingali, S. V.; Schlossman, M. L. Molecular Ordering and Phase Transitions in Alkanol Monolayers at the Water-Hexane Interface. *J. Chem. Phys.* **2004**, *120*, 11822−11838.

(47) Schlossman, M. L.; Tikhonov, A. M. Molecular Ordering and Phase Behavior of Surfactants at Water-Oil Interfaces as Probed by X-Ray Surface Scattering. *Annu. Rev. Phys. Chem.* **2008**, *59*, 153−177.

(48) Tamam, L.; Pontoni, D.; Sapir, Z.; Yefe, S.; Sloutskin, E.; Ocko, B. M.; Reichert, H.; Deutsch, M. Modification of Deeply Buried Hydrophobic Interfaces by Ionic Surfactants. *Proc. Natl. Acad. Sci. U.S.A.* **2011**, *108*, 5522−5525.

(49) Gurtovenko, A. A.; Vattulainen, l. Effect of Nacl and Kcl on Phosphatidylcholine and Phosphatidylethanolamine Lipid Membranes: Insight from Atomic-Scale Simulations for Understanding Salt-Induced Effects in the Plasma Membrane. *J. Phys. Chem. B* **2008**, *112*, 1953−1962.

(50) Small, D. M. Potpourri: Effects of Unsaturation on Lipid Structure; Plasma Cholesterol Ester and Lipid-Transfer Proteins; and Cholesterol-Sensing Proteins and Cellular Cholesterol Movement. *Curr. Opin. Struct. Biol.* **1998**, *8*, 413−416.

(51) McConnell, H. M. Structures and Transitions in Lipid Monolayers at the Air-Water Interface. *Annu. Rev. Phys. Chem.* **1991**, *42*, 171.

(52) Nagle, J. F.; Tristram-Nagle, S. Structure of Lipid Bilayers. *Biochim. Biophys. Acta* **2000**, *1469*, 159−195.

(53) Tronin, A.; Chen, C.-H.; Gupta, S.; Worcester, D.; Lauter, V.; Strzalka, J.; Kuzmenko, I.; Blasie, J. K. Structural Changes in Single Membranes in Response to an Applied Transmembrane Electric Potential Revealed by Time-Resolved Neutron/X-Ray Interferometry. *Chem. Phys.* **2013**, *422*, 283−289.

(54) Hou, B. Ion Distributions at Electrified Liquid-Liquid Interfaces: Microscopic and Macroscopic Measurements. Ph.D. Thesis, University of Illinois at Chicago, 2011.

(55) Grahame, D. C. The Electrical Double Layer and the Theory of Electrocapillarity. *Chem. Rev.* **1947**, *41*, 441−501.

(56) Samec, Z. Electrical Double Layer at the Interface between Two Immiscible Electrolyte Solutions. *Chem. Rev.* **1988**, *88*, 617.

(57) Laanait, N.; Yoon, J.; Hou, B.; Vanysek, P.; Meron, M.; Lin, B.; Luo, G.; Benjamin, I.; Schlossman, M. L. Communications: Monovalent Ion Condensation at the Electrified Liquid/Liquid Interface. *J. Chem. Phys.* **2010**, *132*, 171101−171101−171101−171104.

(58) Laanait, N.; Mihaylov, M.; Hou, B.; Yu, H.; Vanysek, P.; Meron, M.; Lin, B.; Benjamin, I.; Schlossman, M. L. Tuning Ion Correlations at an Electrified Soft Interface. *Proc. Natl. Acad. Sci. U.S.A.* **2012**, *109*, 20326−20331.

(59) Hou, B.; Laanait, N.; Yu, H.; Bu, W.; Chen, C.-H.; Yoon, J.; Lin, B.; Luo, G.; Vanysek, P.; Schlossman, M. L. Ion Distributions at the Water/1,2-Dichloroethane Interface: Potential of Mean Force Approach to Analyzing X-Ray Reflectivity and Interfacial Tension Measurements. *J. Phys. Chem. B* **2013**, *117*, 5365−5378.

(60) Hard, S.; Hamnerius, Y.; Nilsson, O. Laser Heterodyne Apparatus for Measurements of Liquid Surface Properties - Theory and Experiments. *J. Appl. Phys.* **1976**, *47*, 2433−2442.

(61) Langevin, D. Light-Scattering from Free-Surface of a Liquid-Crystal near 2nd Order Nematic-Smectic-A Phase-Transition. *J. Phys. (Paris)* **1975**, *36*, 745−748.

(62) Zhang, Z. H.; Tsuyumoto, I.; Takahashi, S.; Kitamori, T.; Sawada, T. Monitoring of Molecular Collective Behavior at a Liquid/Liquid Interface by a Time-Resolved Quasi-Elastic Laser Scattering Method. *J. Phys. Chem. A* **1997**, *101*, 4163−4166.

(63) Trojanek, A.; Krtil, P.; Samec, Z. Quasi-Elastic Laser Light Scattering from Thermally Excited Capillary Waves on Polarised Liquid | Liquid Interfaces Part 1: Effects of Adsorption of Hexadecyltrimethylammonium Chloride at the Water | 1,2-Dichloroethane Interface. *J. Electroanal. Chem.* **2001**, *517*, 77−84.

(64) Agranovich, V. M.; Loudon, R. *Surface Excitations*; North-Holland: Amsterdam; New York, 1984.

(65) Langevin, D. *Light Scattering by Liquid Surfaces and Complementary Techniques*; Marcel Dekker Inc.: New York, 1992.

(66) Jorgensen, W. L.; Chandrasekhar, J.; Madura, J. D.; Impey, R. W.; Klein, M. L. Comparison of Simple Potential Functions for Simulating Liquid Water. *J. Chem. Phys.* **1983**, *79*, 926−935.

(67) Phillips, J. C.; Braun, R.; Wang, W.; Gumbart, J.; Tajkhorshid, E.; Villa, E.; Chipot, C.; Skeel, R. D.; Kale, L.; Schulten, K. Scalable Molecular Dynamics with Namd. *J. Comput. Chem.* **2005**, *26*, 1781−1802.

(68) Klauda, J. B.; Venable, R. M.; Freites, J. A.; O'Connor, J. W.; Tobias, D. J.; Mondragon-Ramirez, C.; Vorobyov, I.; MacKerell, A. D.; Pastor, R. W. Update of the Charmm All-Atom Additive Force Field for Lipids: Validation on Six Lipid Types. *J. Phys. Chem. B* **2010**, *114*, 7830−7843.

(69) Servantie, J.; Gaspard, P. Methods of Calculation of a Friction Coefficient: Application to Nanotubes. *Phys. Rev. Lett.* **2003**, *91*.

(70) Feller, S. E.; Zhang, Y. H.; Pastor, R. W. Computer-Simulation of Liquid/Liquid Interfaces 2. Surface-Tension Area Dependence of a Bilayer and Monolayer. *J. Chem. Phys.* **1995**, *103*, 10267−10276.

(71) Humphrey, W.; Dalke, A.; Schulten, K. VMD: Visual Molecular Dynamics. *J. Mol. Graphics Modell.* **1996**, *14*, 33−38.

(72) Darden, T.; York, D.; Pedersen, L. Particle Mesh Ewald - an N.Log(N) Method for Ewald Sums in Large Systems. *J. Chem. Phys.* **1993**, *98*, 10089−10092.

(73) Gumbart, J.; Khalili-Araghi, F.; Sotomayor, M.; Roux, B. Constant Electric Field Simulations of the Membrane Potential Illustrated with Simple Systems. *Biochim. Biophys. Acta* **2012**, *1818*, 294−302.

(74) Samec, Z. Electrochemistry at the Interface between Two Immiscible Electrolyte Solutions. *Pure Appl. Chem.* **2004**, *76*, 2147−2180.

(75) Girault, H. H.; Schiffrin, D. J. Adsorption of Phosphatidylcholine and Phosphatidylethanolamine at the Polarized Water/1,2-Dichloroethane Interface. *J. Electoanal. Chem.* **1984**, *179*, 277.

9333

dx.doi.org/10.1021/jp5098525 | *J. Phys. Chem. B* 2015, 119, 9319−9334

(76) Yoshida, Y.; Maeda, K.; Shirai, O. The Complex Formation of Ions with a Phospholipid Monolayer Adsorbed at an Aqueous | 1,2-Dichloroethane Interface. *J. Electroanal. Chem.* **2005**, *578*, 17−24.

(77) Chesniuk, S. G.; Dassie, S. A.; Yudi, L. M.; Baruzzi, A. M. Electrochemical Study of the Interaction of Alkali and Alkaline-Earth Cations with a Dibehenoyl Phosphatidylcholine Monolayer at the Water/1,2-Dichloroethane Interface. *Electrochim. Acta* **1998**, *43*, 2175−2181.

(78) Lewis, B. A.; Engelman, D. M. Lipid Bilayer Thickness Varies Linearly with Acyl Chain Length in Fluid Phosphatidylcholine Vesicles. *J. Mol. Biol.* **1983**, *166*, 211−217.

(79) Luo, G.; Malkova, S.; Yoon, J.; Schultz, D. G.; Lin, B.; Meron, M.; Benjamin, I.; Vanysek, P.; Schlossman, M. L. Ion Distributions near a Liquid-Liquid Interface. *Science* **2006**, *311*, 216−218.

(80) Yu, H. Modulation of Lipid Monolayer and Protein-Lipid Binding under Electric Fields. Ph.D. Thesis, University of Illinois at Chicago, 2014.

(81) Parratt, L. G. Surface Studies of Solids by Total Reflection of X-Rays. *Phys. Rev.* **1954**, *95*, 359−369.

(82) Marcus, Y. Ionic Radii in Aqueous Solutions. *Chem. Rev.* **1988**, *88*, 1475−1498.

(83) Frisch, M. J.; et al. *Gaussian 03*, revision C.02; Gaussian, Inc.: Pittsburgh, PA, 2004.

(84) Small, D. M. Phase Equilibria and Structure of Dry and Hydrated Egg Lecithin. *J. Lipid Res.* **1967**, *8*, 551−557.

(85) Armen, R. S.; Uitto, O. D.; Feller, S. E. Phospholipid Component Volumes: Determination and Application to Bilayer Structure Calculations. *Biophys. J.* **1998**, *75*, 734−744.

(86) Gurtovenko, A. A.; Vattulainen, I. Calculation of the Electrostatic Potential of Lipid Bilayers from Molecular Dynamics Simulations: Methodological Issues. *J. Chem. Phys.* **2009**, *130*, 215107.

(87) Vermeer, L. S.; de Groot, B. L.; Reat, V.; Milon, A.; Czaplicki, J. Acyl Chain Order Parameter Profiles in Phospholipid Bilayers: Computation from Molecular Dynamics Simulations and Comparison with 2h Nmr Experiments. *Eur. Biophys. J.* **2007**, *36*, 919−931.

(88) Small, D. M. *The Physical Chemistry of Lipids*; Plenum: New York, 1986.

(89) Israelachvili, J. N. *Intermolecular and Surface Forces: With Applications to Colloidal and Biological Systems*; Academic Press: London; Orlando, FL, 1985.

(90) Thoma, M.; Schwendler, M.; Baltes, H.; Helm, C. A.; Pfohl, T.; Riegler, H.; Mohwald, H. Ellipsometry and X-Ray Reflectivity Studies on Monolayers of Phosphatidylethanolamine and Phosphatidylcholine in Contact with N-Dodecane, N-Hexadecane, and Bicyclohexyl. *Langmuir* **1996**, *12*, 1722.

(91) Sun, W.; Suter, R. M.; Knewtson, M. A.; Worthington, C. R.; Tristram-Nagle, S.; Zhang, R.; Nagle, J. F. Order and Disorder in Fully Hydrated Unoriented Bilayers of Gel-Phase Dipalmitoylphosphatidylcholine. *Phys. Rev. E* **1994**, *49*, 4665−4676.

(92) Safran, S. A. *Statistical Thermodynamics of Surfaces, Interfaces, and Membranes*; Addison-Wesley Publishing Co.: Reading, MA, 1994.

(93) Luo, G.; Malkova, S.; Pingali, S. V.; Schultz, D. G.; Lin, B.; Meron, M.; Benjamin, I.; Vanysek, P.; Schlossman, M. L. Structure of the Interface between Two Polar Liquids: Nitrobenzene and Water. *J. Phys. Chem. B* **2006**, *110*, 4527−4530.

(94) Daillant, J.; Bosio, L.; Benattar, J. J.; Meunier, J. Capillary Waves and Bending Elasticity of Monolayers on Water Studied by X-Ray Reflectivity as a Function of Surface Pressure. *Europhys. Lett.* **1989**, *8*, 453−458.

(95) Mashaghi, A.; Partovi-Azar, P.; Jadidi, T.; Nafari, N.; Maass, P.; Tabar, M. R. R.; Bonn, M.; Bakker, H. J. Hydration Strongly Affects the Molecular and Electronic Structure of Membrane Phospholipids. *J. Chem. Phys.* **2012**, *136*.

(96) Klingler, J. F.; Mcconnell, H. M. Field-Gradient Electrophoresis of Lipid Domains. *J. Phys. Chem.* **1993**, *97*, 2962−2966.